ABSTRACT

Title of dissertation: CREATING LOCALIZED AMYLOID NUCLEATION
                         OF SILK-ELASTIN-LIKE PEPTIDE POLYMER
                         USING ATOMIC FORCE MICROSCOPY

                         by Brian Matthew Stock, Master of Science, 2015

Directed by: Assistant Research Professor Joonil Seog
                         Materials Science and Engineering

Research into amyloids was initially motivated by pathogenic amyloids involved in disease states such as Alzheimer's; however, new research implicates small oliogmeric species and not the mature fibers. This lack of toxicity has allowed for the development of amyloid-based biomaterials for use as nanowires, biosensors, and tissue regeneration. The directed self-assembly of peptides into amyloid-like fibers for use as biomaterials requires the ability to control both the nucleation location and growth direction of the fiber. We have used Atomic Force Microscopy to repeatedly stretch Silk–Elastin–Like Peptide Polymer (SELP) in the normal direction using continuous pulling in a force acquisition mode which has the ability to create nanodots of SELP at a specified location which are capable of nucleating SELP nanofibers. This work, if generalized to other amyloidogenic systems, may aid in the mechanistic understanding of the assembly process of both pathogenic and functional amyloids.

CREATING LOCALIZED AMYLOID NUCLEATION
OF SILK-ELASTIN-LIKE PEPTIDE POLYMER
USING ATOMIC FORCE MICROSCOPY

by

Brian Matthew Stock

Thesis submitted to the Faculty of the Graduate School of the
University of Maryland, College Park in partial fulfillment
of the requirements for the degree of
Master of Science
2015

Advisory Committee:
Assistant Research Professor Joonil Seog, Chair/Advisor
Professor Robert Briber
Associate Professor Jeffery B. Klauda

Dedication

To my family, Carrie and Aleria, without whom I would have never had the strength to keep going.

Acknowledgments

First I would like to extend my gratitude to Professor Joonil Seog for the hours and hours of discussion of my project, for always asking the tough questions, and for always being understanding of my situation, and for helping me to learn as much about myself in this process as I did about science.

I would also like to thank Professors Robert Briber and Jeffery Klauda for serving on my committee.

Professor Sergei Sukharev and Star Jackson deserve special recognition for helping to guide me through the process of getting a Masters when that option did not exist in the Biophysics program.

I would like to acknowledge all the lab members that have helped me during this time: Nitinun Varongchayakul for training me initially on the AFM and providing a foundation for this work; Eddy Salgado for helpful discussion about AFM and for all the help fixing the AFM when it broke; special thanks to Elliot Bartis for all of his help with ellipsometry; and, lastly I thank Amy Lee for all the helpful discussions about my data.

Finally the undergraduates, Louis Born and Zachary Pelczar for all of their hard work at data analysis and helpful discussions and helping me to understand AFM more deeply by having to train them in the use of the instrument.

Table of Contents

v

List of Tables

List of Figures

Chapter 1:   Background

1.1   Amyloid

Amyloid, originally referring to starch, now refers to the self-assembly of extended fiber structures accessible to most proteins which has parallel or anti-parallel β-sheets or strands stabilized by hydrogen bonds, referred to as cross-β structure [1]. Pauling and Cory showed via X-ray diffraction data of silk fibroin and β-keratin in 1950s and proposed a repeating GXGXG sequence that would give rise to the observed cross-β structures [2, 3].

This cross-β structure is a thermodynamically favorable state along with amorphous aggregates, having a lower free energy than partially or natively folded proteins due to being stabilized by intermolecular interactions driven by hydrophobic forces between portions of the protein exposed in their partially folded state [4]. Even though these amorphous aggregates and amyloid fibers represent the lowest energy state, the presence of molecular crowding within the cell along with chaperones stabilize the native state the protein or direct the folding process to prevent aggregation [4] and the ordered structure of amyloid fibers typically only occurs under certain enviromental conditions for a given protein.

Research into amyloids was initially motivated by pathogenic amyloids formed

by proteins associated with diseases such as Alzheimers or Parkinsons; however, recent research suggests that fibers themselves are non-cytotoxic, but it is instead small oligomeric and pre-fibrillar species which induce toxicity [5,6]. The evidence that amyloid fibers are benign is supported by the presence of so-called "functional amyloids" such as Pmel17 fibers which are thought to aid in melanin synthesis [7,8] or control release of hormones from deposits in the pituitary gland [9]. The lack of toxicity has allowed for the development of amyloid-based biomaterials, such as drug delivery using SELP-47K films [10].

1.2   Silk-Elastin-Peptide Polymer

Our work focuses on a model amyloid peptide Silk-Elastin-Like Peptide Polymer (SELP) consisting of repeating silk-like (GAGAGS) and elastin-like (GVGVP) blocks that provides both the mechanical stability of silk and aqueous solubility of elastin [11]. SELP is produced using DNA recombinant technology and consists of silk-like blocks (Gly-Ala-Gly-Ala-Gly-Ser) which mimic the repeat unit of *Bombyx mori*(silkworm) silk and elastin-like blocks composed of (Gly-Val-Gly-Val-Pro) from mammalian elastin [11]. SELPs are referred to herein by number of silk-like blocks followed by the number of elastin like blocks. SELPs consisting of both 8 silk-like blocks, 15 elastin-like blocks, and 1 lysine modified elastin-like block (Gly-Lys-Gly-Val-Pro) (815K) or 4 silk-like blocks, 7 elastin-like blocks, and 1 lysine modified elastin-like block (47K) were used. The polymer chain consists of a head, six SELP units (815K) or 13 SELP units (47K), and a tail, giving a molecular weight of 65,374

Da and 69,814 Da for 815K and 47K respectively [11].

The complete amino acid sequence of 815K is MDPVVLQRRDWENPGVTQL NRLAAHPPFASDPM[GAGS(GAGAGS)$_2$(GVGVP)$_4$GKGVP(GVGVP)$_{11}$(GAGAGS)$_5$ GAGA]$_6$MDPGRYQDLRSHHHHHH.

The complete amino acid sequence of 47K is MDPVVLQRRDWENPGVTQL NRLAAHPPFASDPMGAGSGAGAGS[(GVGVP)$_4$GKGVP(GVGVP)$_3$(GAGAGAGS)$_4$]$_{12}$ (GVGVP)$_4$GKGVP(GVGVP)$_3$(GAGAGS)$_2$GAGAMDPGRYQDLRSHHHHHH.

SELPs can form biocompatible fiber mats and at higher concentrations that have been shown to support adhesion of human fibroblasts with no cytoxicity [12] as well as undergo a sol-gel transition at 37°C which has been studied for use with drug delivery applications [11, 13].

This work, however, focuses on understanding the fundamental assembly process of SELPs at significantly lower concentrations than those used to create fiber mats or other hydrogel materials where we have the ability to monitor the assembly process in situ on a mica surface using Atomic Force Microscopy (AFM) in an effort to observe the heterogeneous oligomeric amyloid precursor states of SELP and their potential evolution into fibers.

Although we have not done X-ray diffraction of SELPs to confirm the pattern of cross-β structure, treatment of SELP-47K films with methanol showed an increase in anti-parallel β-sheets by FT-IR and Raman spectroscopy consistent with a Silk I to Silk II transition [14] which implies that the silk-like GAGAGS regions of the fibers are likely forming these β-sheets. While SELP-47K may be classified as amyloid-like, we will refer to SELP nanofibers as amyloid throughout the text for clarity

but with the knowledge that the formed fiber structures without detailed structural information may not be true amyloid fibers.

1.3   Amyloid Nucleation

Growth of amyloid fibers in a nucleation-dependent polymerization model divided into three phases: a lag phase containing momomers and other non-nucleating species; a growth phase in which self-assembly occurs rapidly; and a plateau phase in which self-assembly slows down as available material is depleted [15]. In classical nucleation theory, the nucleus is a thermodynamically unfavorable state of some critical size which must be formed before additional growth can occur making nucleation the rate-limiting event under this type of aggregation. The lag phase can be long, as in Tau which is on the order of days [16] to months [17] depending on environmental conditions, or as in the case SELP, essentially no lag phase when assembled on a mica surface [18].

Whereas most amyloid nucleation is induced by environmental changes such as salt, pH, or temperature, it can also be induced mechanically as we have shown in our previous work and it is that mechanically induced nucleation which is the focus of this current work.

1.4   Mechanically Induced Amyloid Fibers

One can look to nature to amyloid fibers being mechanically induced such as the dragline and capture silks produced by spiders or the cocoons of silk worms.

While silk solutions can be wet–spun into macroscopic structures, we are interested in both creating fiber patterns on a smaller scale and understanding the nucleation and grow behavior of the resultant fibers. By using SELP on mica surfaces, the lag phase is essentially eliminated and we can observe the nucleation process *in situ* with AFM by inducing fiber growth with the AFM tip.

Manipulation of protein surfaces by AFM tips was observed as early as 1992 by Lea et al. [19] when imaging IgM deposited on mica during which they saw alignment of strands of IgM attributed to be oriented parallel to the angle of the tip relative to the scanning direction as well as increased surface coverage of the protein after repeated scanning. They also attempted patterning of fibrinogen absorbed onto mica and saw either sweeping of the protein to the edges of scanning area at high (>30 nN) forces, but were able to align strands of fibrinogen and observe an increase in height over scanned areas to form a 'U' in a 10 μm area when scanning at 30 nN, and observed no change to the surface at 4 nN of tapping force.

The literature on mechanically induced nucleation and growth of nanofibers, however, is largely limited to macroscopic techniques such as agitation in an eppendorf shaker [20], shear-flow [21,22] and sonication [23,24].

One recent example of mechanically induced nucleation and growth at the nanoscale is Zhong et al. [25] who created micropatterns of silk fibroin (SF) protein on mica by both tapping and contact mode scanning with the tip inducing the absorption of the SF onto the mica over a timescale of hours. They attributed the deposition to a sol-gel transition of the SF caused by either tip oscillations in tapping mode or shear force in contact mode.

5

Yang et al. [26] showed that an ionic-complementary peptide EAK16-II, sequence AEAEAKAKAEAEAKAK and EFK16-II, sequence FEFEFKFKFEFEFKFK which self-assembled on both mica and highly-ordered pyrolytic graphite (HOPG) when scanned with an AFM tip in tapping mode. Here the authors argue that AFM tip is fragmenting the peptide and that those fragments act as "seeds" by providing additional "active ends" for new nanofiber growth. They also showed preferential detachment of the peptide in 10 mM HCl which was used to create hydrophobic strips of HOPG on peptide covered surface.

Mechanically induced nucleation and growth were also shown by Zhang et al. [27] using GAV-9 peptide, sequence $NH_2-VGGAVVAGV-CONH_2$ [28]. GAV-9 epitaxially assembles on both mica and HOPG, forming flat tapes on HOPG and in an upright orientation for form fibrils on mica [28] that can further assemble into multilayer structures based upon the salt concentration [29]. By pushing on a GAV-9 fiber new growth could be directed along mica lattice and defects could be repaired by removing the defect with scanning and allowing the fiber to self-heal in low concentration monomer solution [27].

Previously in our lab we have shown that SELP self–assembles on mica surfaces with little or no lag phase [18]. Following this, Chang et al. showed that this self–assembly can be accelerated by the mechanical stimulus provided by the AFM during tapping mode imaging and that increasing the peak tapping force by increasing the free amplitude resulted in increased nucleation of fibers on the SELP–815K coated mica surface [30]. Interestingly, pre–formed fibers on the mica surface showed no clear preference in their orientation whereas 80% of fibers created as a result of

mechanical stimulus were oriented between 60 and 90°with respect to the scanning direction.

Next, Johnson et al. showed that increasing line density and decreasing scanning speed resulted in greater fiber coverage and succeeding in creating micropatterns of SELP fibers with directional control [31]. They additionally observed that if more nucleation sites were created within the first scan, subsequent scans would result in less nucleation indicating a competition between nucleation and elongation processes with the limited amount of SELP material absorbed onto the mica surface.

Most recently Varongchayakul et al. showed that nucleation results from lateral stretching of either individual or networks of SELP molecules [32] and that nucleation occurred more readily for exponential force profiles which were the result of stretching a network of SELP molecules. Time–lapse Lateral Force Microscopy (LFM) was used to increase the temporal resolution and allowed for the observation of a step–wise height increase of SELP fibers after nucleation occurred during the contact mode scanning. This lateral force technique can be used to pattern a single nanofiber; however, the nucleation location of that fiber is random with respect to the line being scanned. The growth direction of force induced SELP nanofibers was, again, preferentially perpendicular to the scanning direction [30, 31] rather than epitaxially oriented along the mica lattice, likely due to the much larger size of SELP-47K or SELP-815K as compared to smaller fiber forming peptides making alignment difficult [32].

Nucleation and growth mechanisms are important to understand in amyloid systems both from a fundamental perspective of studying the important early stages

of amyloidogenesis as well as being able to control the nucleation and growth of the resultant fibers for use in novel amyloid biomaterials. Johnson et al. speculated that the ability AFM tip to nucleate SELP in tapping mode was a result of the molecule being stretched and compressed by the oscillatory motion of the AFM tip [31]. Knowing that lateral force alone could nucleate fibers, we have decided to explore the potential of using tapping-mode as well as mimicking tapping-mode with force curves in order to better control the nucleation location of the SELP nanofibers. This work aims to gain better control over that nucleation process using SELP-47K and SELP-815K and a force-curve based approach.

Chapter 2:   Creation of Nanodots with AFM

2.1   Introduction

There are several examples in the literature of patterning techniques for proteins ranging from traditional Dip-Pen Nanolihography (DPN) [25] and aqueous DPN approaches [33] to microcontact printing of protein via Ni(II)-mediated histidine interactions [34]. Zhong et al. showed that hydrophobic silk fibroin protein can be micropatterned onto a mica surface via a tip-induced process [35].

By using a continuous pulling force curve method to induce nucleation, we have reduced the location of fiber nucleation to 50-100 nm which is nearly an order of magnitude improvement over the lateral force technique, but with the probabilistic nature of SELP amyloid fiber nucleation induced via mechanical stretching it appears that formation of a nucleus is more difficult under these conditions as compared to the lateral stretching method. This technique differs from Dip–Pen Nanolithography (DPN) or Polymer–Pen Lithography(PPL) approaches in that it is the presence of molecular stretching that determines the creation of a nanodots and is largely independent of the dwell time of the tip on the surface and the normal (trigger) force (data not shown) whereas with DPN larger forces and longer dwell times lead to larger surface features [36]. We cannot discount the possibility that

longer dwells or higher forces deposit more material; however, the lack of measurable changes to the topography of patterned area imply that either no material is deposited during these times or that the deposited material is highly diffusive on the mica surface and as such is not possible to image.

This technique allows for the creation of both small oligomeric clusters of SELP (henceforth referred to as nanodots) that sample configurations that both allow and disallow the growth of fibers from these nanodots. A heterogenous population of intermediate species is consistent with the early stages of other amyloidogenic systems [7]. The nanodots that are in a fiber competent configuration appear to be further sub-divided into those that spontaneously grow into fibers and those that require being scanned by the AFM tip before nucleating into fibers.

2.2   Methods

2.2.1   Atomic Force Microscopy

AFM is a well-established technique to determine both topography and mechanical properties of surfaces. Our AFM, an Asylum MFP-3D (Oxford Instruments), uses an 860 nm super-luminescent diode (SLD) which is focused onto a cantilever beam. The light from the SLD is reflected, collimated, and reflected again by an adjustable mirror and collected on the position-sensitive diode (PSD) where vertical movement corresponds to deflection of the cantilever in the normal direction and horizontal movement corresponds to lateral deflection (bending) of the cantilever.

In AC or tapping-mode, the cantilever is acoustically driven by a shake piezo where the cantilever oscillates at a given amplitude which is maintained through feedback on the Z-position. The larger the difference between the amplitude setpoint and free amplitude, the larger the force exerted on the sample, therefore ideally the smallest amplitude possible should be used to maintain image quality. Typically, amplitudes of 70-80% of free amplitude (tuned to 400 mV) were used, which gives an oscillation amplitude of 35-40 nm for typical lever sensitivity.

Since the feedback strives to maintain a constant amplitude, strong surface interactions can affect the measured height and introduce artifacts. This is typically observed for certain samples where nanodots appear to have heights ranging from 30 to 100 nm and is likely a result from the attractive forces on those sample surfaces which pulls the AFM tip downwards, causing the feedback to compensate by moving the Z-piezo upwards and so the attractive force is seen as an increase in height. Avoiding this artifact is difficult as it is not always possible to return to the same area with a different tip to image the nanodots, nor are some nanodots stable enough to do so. The practical result of this is that nanodot heights are not taken as an absolute measure of feature height, but relative height differences for nanodots created under different conditions can be measured relative to fiber heights imaged with the same tip.

Another way to mitigate the discrepancy in nanodot height, is to image the nanodots in contact mode, where a constant deflection (normal force) of the cantilever is maintain as the tip is dragged along the surface. In cases where the nanodots can be imaged in contact the height can simply be compared and in the

presence of the tapping artifact, the height should be significantly lower. However, certain nanodots appear to be swept away by the tip even at the lowest contact forces of 100 pN which makes this a difficult way to double-check the heights of the nanodots.

Since morphology of the nanodots is difficult to assess with AFM due to strong tip-sample interactions, some understanding of the differences between the nanodots can be obtained using the force curves used to create them. The particular features of the force curves will be discussed in Chapter 4 and the continuous force method will be discussed in detail in the relevant section below.

Fiber widths are obtained by calculation of the full-width at half-maximum (FWHM) from a Gaussian fit of a trace drawn across the fiber using the Igor Pro software. This is done to de-convolute the tip broadening effect from the width of the fiber and obtain an accurate measure of the fiber width. Fiber heights are easily obtained from Gaussian fitting of the histograms of height at each point of trace drawn along the fiber.

2.2.2   Substrate Preparation

Muscovite Mica, in pre-stamped 9.9 mm discs (Ted Pella, Inc.) were affixed to glass microscope slides using a 5-minute epoxy and allowed to cure at room temperature for at least four hours but typically overnight. Mica was freshly cleaved with adhesive tape before use.

For all experiments with coated tips and for bare tip on bare mica controls, 80

μL of MilliQ water was dropped onto the mica substrate. For experiments involving a SELP-coated mica, 40 μL of the appropriate SELP stock was deposited on the surface and allowed to incubate at room temperature in a humid chamber (petri dish with wet filter paper) for at least 30 minutes to overnight before washing three times with 80 μL of MilliQ water and leaving in 80 μL of MilliQ water for at least two hours after washing before imaging. Samples that were not allowed to rest after washing appeared to have an unstable protein surface and were difficult to image with any reasonable quality. For dried and re-hydradrated samples, the SELP-47K surface was first imaged and force curves were taken and then the sample was allowed to dry for eight hours after which it was re-hydrated with 80uL of MilliQ water and allowed to re-hydrate for at least four hours before imaging. Trying to re-hydrated and image immediately resulted in unstable surfaces that were not able to be imaged with any reasonable quality.

2.2.3 Tip Preparation

Silicon nitride tips on rectangular silicon nitride cantilevers (MLCT, Bruker) were used for all experiments. The resonate frequency was typically 8-9 kHz in water. The spring constant was calibrated using the thermal tuning method for all cantilevers used. The spring constant was typically 20 pN/nm.

Initially, unused tips were scanned repeatedly on a SELP coated mica surface to coat the tip after which it was engaged on bare mica and single force curves were used to create nanodots at specific locations. This method provided a high

yield of nanodots; however, after discovering that these tips could produce artifacts (discussed below) this method was abandoned for a different coating procedure that began by UV/Ozone cleaning the tips. The UV/Ozone cleaning removed the possibility for the creation of artifacts, but had the unfortunate side–effect of reducing the ability to create nanodots.

Before use all tips were UV/Ozone cleaned for 15 minutes and either used directly or were placed in petri dish and the end of the probe where the cantilever of interest was located was covered in a 20 μL droplet of SELP stock and allowed to dry under vacuum for 1 hour before use. Tips coated in this way were usable for up to week after preparation.

2.2.4   AFM Parameters

Images were typically collected with 1024 points and 512 scan lines at 1.78 Hz scan rate unless otherwise noted. Tapping mode setpoints were typically $\sim$75% of free amplitude which corresponds to about a 4 nN peak tapping force according the simulation software developed by Prof. Santiago Solares [37]. Contact mode imaging was carried out at 90° scan angles so that lateral force microscopy (LFM) data could be collected. Contact imaging was done to minimize the contact force which was typically a 50 mV relative setpoint which corresponds to normal force of approximately 100 pN.

2.2.5   Continuous Force Mode Method

Using the inverse optical lever sensitivity or InvOLS, one can determine the amplitude of the cantilever in nm, which for the setpoints used is approximately 25-30 nm depending on the InvOLS value. We hypothesized that perhaps a combination of the multiple taps at single point [38] along with the point density along a scan line making each scan point significantly smaller than the typical tip radii of MLCT tips of 50nm as determined by SEM (see Section 3.5) meant that tip could be picking up a molecule of SELP and stretching and compressing it multiple times and that this may be the underlying cause of mechanically induced nucleation in tapping mode. We then set to mimic tapping mode by using force curves which had been typically taken using a force distance (the distance that tip retracts) of 1000 nm which is nearly three times the contour length of SELP–47K. By reducing the force distance to values below the contour length (300, 250, 200, 150, and 100nm) we were able to observe what we believe to be tethering of the SELP molecule between the mica and tip surfaces. Although not always successful, this tethering behavior is always present (with one possible exception, see Section 4.3) for force curves that result in the creation of nanodots which are able to grow into amyloid fibers.

To get an estimate of the number of taps at a given scanning point we can treat the contact radius of tip as if the tip were a spherical cap with radius of 50 nm and height of 1 nm which gives a contact radius of 10 nm meaning the diameter is 20 nm or 20 points in a 2000 nm scan line at 1024 points per line. If we then allow for multiple taps at each point and take into account the overlap each point

is tapped 8 to 24 times, thus we choose 10 and 20 total curves as the limits of the continuous pulling.

Trigger forces were 100 pN or 200 pN and dwell times varied from 1 to 10 seconds; however, these parameters had little effect on the force behavior and the resulting nucleation and dwell times of 1 or 2 seconds were sufficient and typically used. This is in contrast to certain nanodots made with SELP–815K in a non-continuous mode where dwell time, but not force, sometimes showed increases in height for increasing dwell times (data not shown).

2.3   Results

2.3.1   Verification of Tip Coating with AFM

Verification that AFM tip is coated with SELP can be done by simply scanning bare mica and observing fiber growth as the only place that material for those fibers could have come from is the coated tip, regardless of the deposition mechanism. This can be seen in Figure 2.1 which demonstrates that fibers can be patterned on a mica surface with a SELP–47 coated tip by disabling the slow–scan axis and scanning a single line over a 1 μm area in tapping mode at 0°. Tapping mode provides the mechanical stimulus to drive the fiber growth and the resultant fibers are perpendicular to the scanning direction. Fibers oriented horizontally in the figure were induced during the scanning and the vertically oriented fibers were mechanically induced during the imaging which was performed at 90°. Additional fibers are induced as the surface is repeatedly scanned with fibers likely growing from material

16

deposited during previous scans. The heights of the fibers created are 3.0 ± 0.2 nm (N = 5) with a FWHM of 28.8 ± 0.4 nm (N = 3) which is consistent with the heights of 1.98 ± 0.01 and 3.4 ± 0.2 nm (N = 27) and FWHM's of 29.5 ± 0.4 nm and 38.5 ± 0.4 nm (N = 27) measured for SELP–47K fibers formed on a SELP–47K coated mica surface and measured in water with tapping mode (data not shown). N refers to the number of fibers measured in each case. The appearance of fibers on the mica surface with no other material present along with consistency of heights and widths of the formed fibers shows that the AFM tip is coated with 47K and that tapping mode can induce fibers with directional control; however, the nucleation location is still limited to appearing randomly within the scan line. Both single force curves as well as continuous pulling at reduced distances are used in the following sections in an attempt to gain better spatial control of the nucleation location.
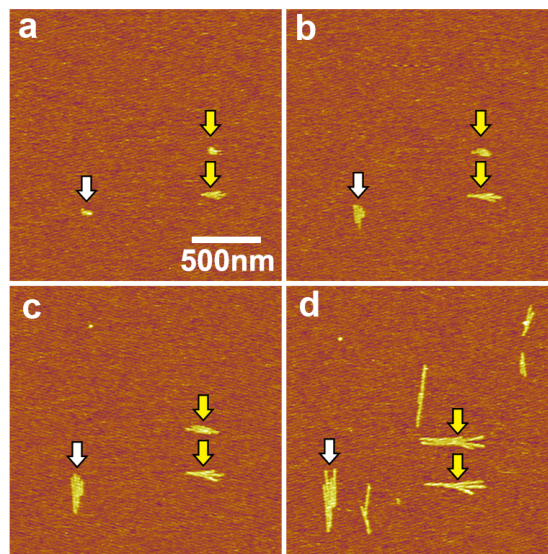
Figure 2.1: Fibers patterned by scanning 1 μm areas with the slow–scan axis disabled in order to scan a single line in tapping mode at 0° and the scanning the area in tapping mode at 90°. The white arrow indicates that fiber growth was initiated by material deposition during the scanning and then mechanically induced at 90° and the yellow arrow indicates fibers that were mechanically induced during the scanning giving, those fibers a growth direction perpendicular to fibers indicated by the white arrow. Images taken at various time points to show the growth of the fibers at a) 0 b) 3 c) 6, and d) 14 minutes. Scale bar in (a) is the same for all images.

2.3.2 Artifacts versus Nanodots

One of the more difficult aspects of AFM is to ascertain whether a particular surface feature is composed of the molecule of interest or is some type of artifact. As can be seen in Figure 2.2 the force curve for an artifact shows no molecular stretching in the extension region of the curve as well as typically having an adhesion (pull-off force) in the 1 nN or greater range compared with the lower adhesion and presence of molecular stretching in the retraction portion of the curve for a

nanodot. The artifacts created in that figure are from an uncoated tip that was not UV/Ozone cleaned and made those features on bare mica. After observing this all tips used thereafter were UV/Ozone cleaned to prevent this behavior. With the presence of lower adhesion or molecular stretching events in the curves, other nanodots created with SELP–815K are likely composed of SELP based on their force behavior. Stretching is also present in the force curves that allowed the creation of the 'NANO' pattern see in Figure 2.3 and the adhesion for those curves was below 1 nN. Therefore, careful inspection of the force curves associated with nanodot creation could, in theory, be used to be able to distinguish between nanodots and artifact. However, even with a reduced ability to pattern with UV/Ozone cleaned tips that have been coated with SELP, it is better to avoid the possibility of artifacts and thus we have chosen to UV/Ozone clean all tips after observing this behavior.
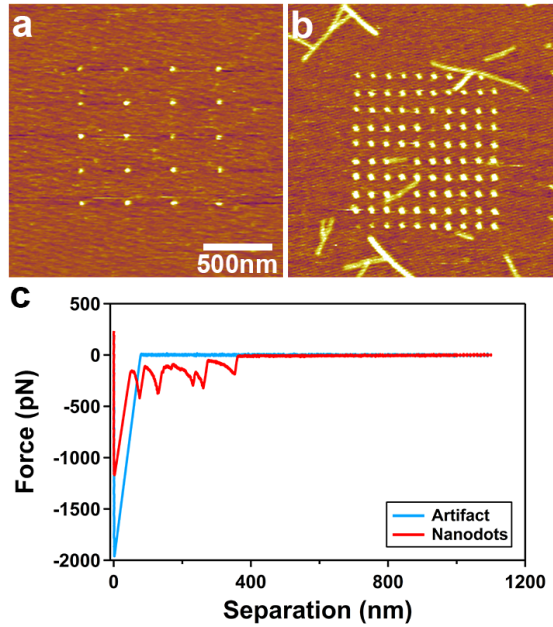
Figure 2.2: a) Artifactual pattern created with a bare tip on bare mica with 100 pN trigger force and 10 s dwell time at the sruface. b) Nanodots created on a SELP–815K surface with a 200 pN trigger force and 10 s dwell time at the surface. c)Representative force curves used to create the nanodots or artifacts.
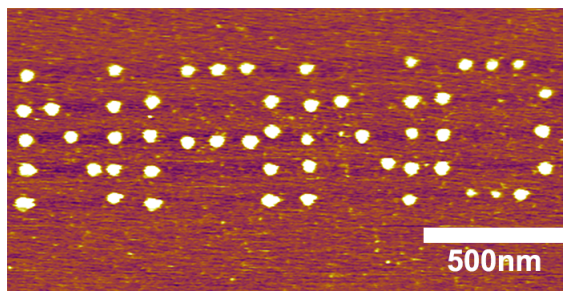
Figure 2.3: Nanodot pattern with 100 nm spacing between nanodots created with SELP–815K using a non–UV/Ozone cleaned tip by taking single force curves with a 100 pN trigger force, 1 s dwell time, and 1000 nm force distance. "Go There" Mode in the AFM software was used to manually draw the pattern where the force curves would be taken.

2.3.3 Factors that Control the Creation of Nanodots

Unlike DPN, dwell time and trigger force have little effect on the apparent nanodot size. Since we are mimicking tapping mode in some sense the number of taps in an area as well as retraction distance before re-approaching the surface should be the critical factors as from tapping mode nucleation we know two things. One, the tip will tap the surface at least one time, but will tap over the same area multiple times even outside of a multiple tapping regime due to the size of tip contact area with the surface. Two, we need to reduce the retraction distance so that we don't break the molecule and allow for subsequent curves to stretch the molecule since we know that stretching is a requirement for the creation of a nucleation site [32].

2.3.4 SELP Fiber Growth from Nanodots

In most cases coated tips used on bare mica surfaces resulted in spontaneous nucleation of fibers, without the need for additional mechanical stimulus via LFM. It is difficult to assess whether the nanodots grow into fibers without the aid of the mechanical stimulus provided by AC imaging as we need to apply that stimulus in order to take the image and assess the resultant morphology. However, as can be seen in Figure 2.4 the fibers growing from the nanodot appear to be oriented randomly, which is typically not the case for fibers that are mechanically induced as fibers that are mechanically induced grow predominately perpendicular to the scanning direction [32].
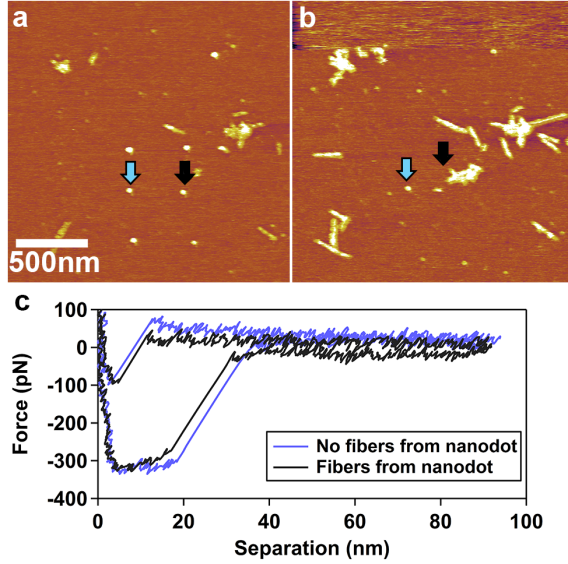
Figure 2.4: a) Nanodot pattern created with 100pN trigger, 2s dwell time, and 20 curves at each point. b) Fiber growth from nanodots after mechanical stimulus. c) Representative continuous mode force curves used to create the nanodots that did not (white arrow) and did (blue arrow) grow into fibers upon mechanical stimulus.

In certain cases such as Figure 2.5, nanodots can be laterally stretched to induce fiber growth and the resultant fiber growth is mostly perpendicular to the scanning direction; however, most nanodots either dissipate or appear to spontaneously grow from the deposited material. Some nanodots also appear to be swept away from the scanning area by either tapping or contact mode scanning (data not shown) and so it is not always possible to apply force directly to the nanodots.
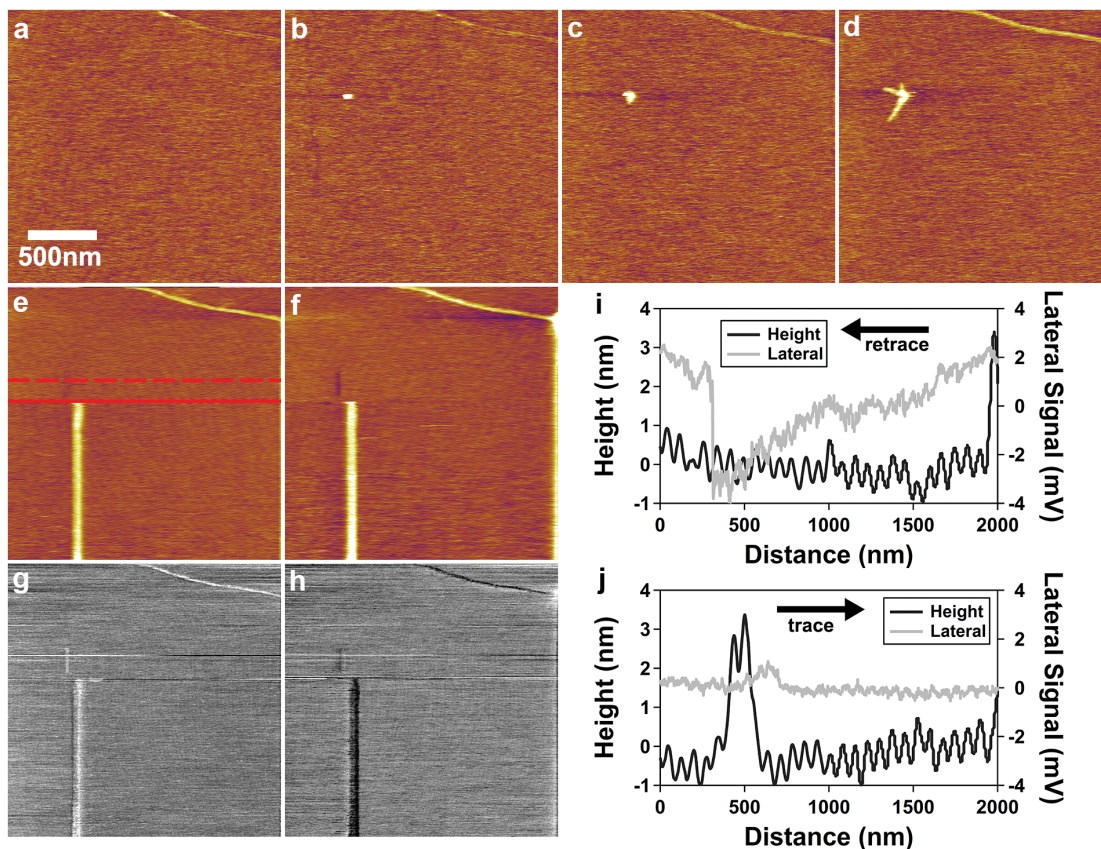
Figure 2.5: a) initial area b) after continuous force mode (10 curves, 1s dwell, 100pN trigger) at location where nanodot was formed c) nanodots immediately after LFM d) 1 hour later shows fiber growth from nanodot.e-h) Lateral force microscopy (LFM) of nanodots. Height trace, height retrace, lateral trace, and lateral retrace contact mode images over nanodot. Red dashed-line in (e) shows location where slowscan axis was disabled. Plots of traces before (i) and after (j) height increase in LFM. Data in plots is located at red solid line in (e) and trace from next scan-line down in the image. Scale bar is the same for all images. Lateral signal is in mV as lateral force was not calibrated.

2.4   Discussion

Starting with the knowledge that only lateral force is necessary to nucleate

SELP fibers on mica and being aware that the mechanical force applied in tapping

23

mode could also induce fiber growth, we sought to explore the ability of tapping mode to gain control of the nucleation location of SELP fibers. Initially, starting by disabling the slow scan axis in order to tap along a single line, we were able to mechanically induce fibers along those lines that grow perpendicular to the scanning direction consistent with our previous results. Single force curves were explored next but tended to produce nanodots that did not act as nucleation sites, some of which were hampered by artifacts.

By using a continuous force mode method, we have created nucleation sites for SELP amyloid fibers at specified locations. However, there are some downsides to this technique. One is the difficulty in reproducibility as factors such as how much SELP is absorbed onto the tip for different coating techniques and/or variances in the tip radii. Better understanding of the absorbed SELP layer as well as knowledge of the tip could mitigate this issue; however, the local concentration and/or the number of molecules that are required to be stretched to create a nucleation location may be a very narrow range. This, in turn could lead to the low probability of creating a nucleation location with this method due to simply not being enough material in 50 nm area as opposed to the material available over a 500 to 2000 nm scan line. Second is the lack of directional control for the fibers that spontaneously grow from certain nanodots, which indicates that, as previously noted [30], the scanning direction of the tip may set the orientation of the fiber whereas fibers that are formed without mechanical stimulus appear to be oriented randomly.

The reduced ability for the tips that were UV/Ozone cleaned may be due to making the tip surface more hydrophilic as SELP is largely hydrophobic with the

lysines providing the electrostatic attraction to the negatively charge tip surface much in the same way SELP binds to the mica surface. Hydrophobic surfaces may induce the SELP to form stable amorphous aggregates due to being able to bind more of the protein to the surface, which would account for both the larger pull-force and for the inability of these nanodots to nucleate into fibers as they are already stabilized by the surface and so the activation barrier to form amyloid is much higher for an oligomeric state that cannot associate as well with the surface to stabilize its conformation. This overall reduction in binding may allow more of the SELP that is dried to the surface to be removed as the tip equilibrates in the water droplet reducing the amount available for patterning.

The following chapters discuss the surface characterization and the force curves obtained from these experiments in an effort better understand the surface that tip interacts with to see whether differences in the force behavior can account for either the spontaneity of fiber growth from nanodots or low probability of creating a nucleation site with this method.

Chapter 3: Surface Thickness and Tip Characterization

3.1 Introduction

Better understanding of the nucleation and growth behavior of SELP fibers must begin with characterization of both the substrate and the AFM tip. The first question is how does the SELP organize on the mica surface and does it form a monolayer of protein or more complex multilayer structure? We hypothesize that lysine in the elastin-like repeats allows SELP to electrostatically bind to the mica surface leaving the silk-like blocks free to self-assemble. This model is reasonable due postive charge of lysine in water and the negatively charged mica surface as well as previous results that show the inhibition of self-assembly with increasing salt for SELP–415K [18]; however, we lack the fine structural data of SELP on the mica surface to verify that model at this time.

Obtaining this surface structure with AFM is challenging as mobile portions of SELP appear blurred when imaging in water, but if the sample is dried then the protein is immobilized and can be imaged and a multi-layered surface structure reminiscent of elastin-like peptide multilayers on HOPG [39] is observed. We look at the results of this air imaging in the first section of this chapter. The second and third sections assess with ellipsometry and AFM how the thickness of these layers

are measured on both silicon, which does not appear to form multilayers, and mica, which can only be assessed with AFM.

The last section discusses the use of Scanning Electron Microscopy (SEM) in an attempt to measure changes in tip radii under various treatments as it is reasonable to expect a increase in tip radii upon drying SELP onto the probe; however, the change is small and no clear differences are found under the various conditions. The goal was to correlate tip radius with the type of features patterned by a given tip, not an effort to verify the coating procedure which can be readily assessed with AFM imaging as previously discussed.

3.2   Observation of layered SELP structures on mica in air

3.2.1   Methods

40μL of 0.5μg/mL SELP–815K in water was deposited onto mica and the surface and allowed to dry under ambient conditions. The surface was imaged using a silicon tip (NCLV) in air using dual-mode AC. In dual-mode, both the first and second eigenmodes of the cantilever are driven in this mode which were 160 kHz and 1000 kHz. We are primarily concerned with the height images in this case so the dual-mode is merely used in attempt to obtain a high resolution image.

For SELP–47K, 40μL of 2μg/mL SELP–47K in water was deposited onto mica and allowed to dry under ambient conditions. The surface was imaged using a silicon nitride tip (MLCT) in air using contact mode. Contact mode in air using a soft cantilever such as this provides comparable (or better) image quality in our

experience with our particular AFM without the additional complexities of dual-mode AC imaging.

For each type of SELP, at least three different areas of a 5 μm image showing the multilayer structure was sampled using the Igor histogram function ignoring areas outside of a masked area so that regions of interest could be sampled. The resultant histograms were fit with a Gaussian function and layer thickness was determined from the difference in the mean height of the sampled area for that layer. Errors are reported as standard deviations.

3.2.2 Results

The multi–layer structure for both SELP–47K and 815K is shown in Figure 3.1. The first layer is either not resolved or represents the mica surface. It is shown as background in the histograms. The next layer appears blurred for 47K and shows small fiber–like structures for 815K. The second layer is likely the diffuse protein layer which appears blurred during normal imaging in fluid. It is upon this layer that fibers and larger amorphous aggregates appear which can be considered their own layer in some sense.

For 815K, the thickness of these layers was 0.7 ± 0.7 and 1.2 ± 0.7 nm for the first and second layers respectively for a total thickness of 2.0 ± 0.8 nm. Force 47K the layer thicknesses were 2.7 ± 1.1 and 3.5 ± 1.3 nm for a total thickness of 6.2 ± 1.2 nm.
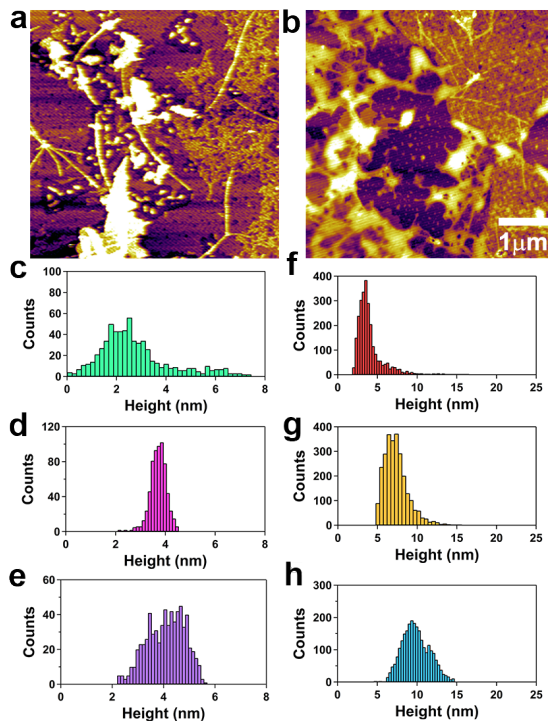
Figure 3.1: Imaging SELP coated mica surface surfaces in air reveals a multilayer surface. a) SELP–815K b) SELP–47K. Representative histograms for the c and f) background (lowest) and d and g) first and e and h) second layer for 815K and 47K respectively.

3.2.3 Discussion

Imaging of SELP surfaces in air revealed a multilayer structure that shows short fibers on the SELP–815K surface that appear oriented epitaxially, although this was not confirmed, followed by a less oriented layer in and on which fibers and aggregates grow and it is likely that second layer than we observed as blurred during imaging in liquid. It is not clear if the lack of the epitaxial layer for SELP–47K surface is simply a result of the image quality for contact mode or due to differences in its multilayer structure. The total layer thickness of 2 nm and 6 nm for SELP–815K

and 47K respectively is just the sum of these two layers and it is this total thickness that we will now compare to the layer thickness as determined by ellipsometry and AFM.

3.3 Determination of SELP Layer Thickness with Ellipsometry

Before determining the layer thickness with AFM, we first wanted to be able to validate the observed protein layer with an alternate technique. We choose ellipsometry because it is an established technique for determining the thickness of thin films and we could prepare samples in similar manner as those for AFM providing a basis of comparison between the two instruments. We did, however, have to prepare SELP samples on silicon substrates due to the optical transparency of mica. We mitigated this downside by also determining the layer thickness using AFM for SELP coated silicon.

3.3.1 Methods

Silicon was diced into 1 cm squares, piranha cleaned with a 7:3 solution of H_2O_2 and H_2SO_4 and then air dried. Once dried, silicon was UV/Ozone cleaned for 5 minutes and then $40\mu L$ of SELP-815K at concentrations of $0.125\mu g/mL$ and $5\mu g/mL$ were deposited and samples were allowed to dry overnight under ambient conditions. UV/Ozone cleaned silicon was used as control and to establish the thickness of the oxide layer formed on the silicon during the cleaning processes which can be seen in Figure 3.2.

A He–Ne ellipsometer (632.8 nm) with an angle of incidence of 72° was used and Ψ–Δ data was fit with a multilayer model, simulated in Excel, to obtain layer thickness. The scanning angle can vary slightly as the sample is moved through the laser and adjustments are made in the simulated data by changing the angle of incidence to obtain a "best–fit" line through the data points. For SiO_2, the layers were air, SiO_2, and Silicon with complex refractive indices of $1 + 0i$, $1.457 + 0i$, and $3.866 - 0.028i$ respectively obtained from literature values [40]. The complex refractive index of SELP used was $1.530 + 0i$ which was determined using a prism coupler by Teng et al. for SELP–47K films [14].
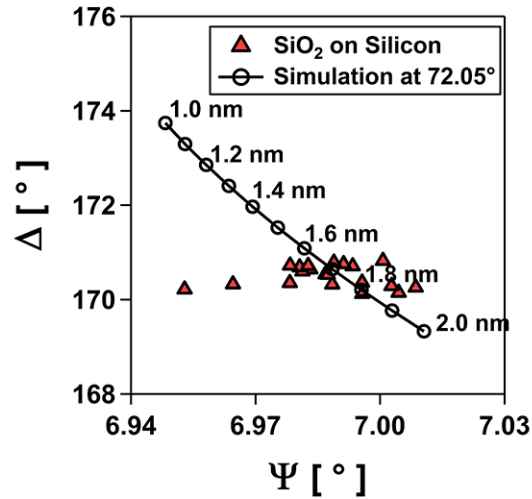
3.3.2 Results

Figure 3.2: Determination of the silicon oxide layer thickness formed during the cleaning process of silicon substrates. The spread in the data is due to variations in the angle of incidence as the substrate is scanned by the laser.

Now that the thickness of the native oxide layer was determined to be 1.8nm, we can add a third layer to the multilayer model with the refractive index of SELP–47K and determined the thickness of the 815K layer on silicon as shown in 3.3 to be between 1.5 to 2.5 nm for the 0.125 μg/mL SELP–815K and between 2.5 to 5 nm for 5 μg/mL SELP–815K on silicon.
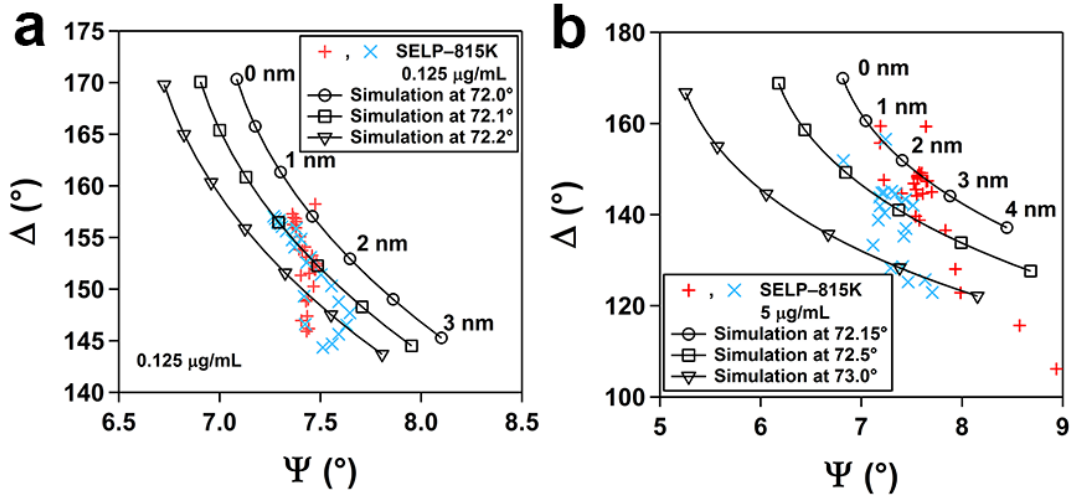
Figure 3.3: Determination of the SELP–815K layer thickness on silicon substrates. The spread in the data is due to variations in the angle of incidence as the substrate is scanned by the laser. The thickness of the oxide layer was taken to be 1.8nm.

3.3.3   Discussion

Based on the observed thickness of the multilayer in air, we should expect SELP–815K layer to be at least 2 to 3 nm as we are using a 10–fold increase in concentration of SELP on the silicon surface. The ellipsometry results show that SELP–815K layer ranges from 2.5 to 5 nm which agrees reasonably well with the AFM air imaging of the SELP on a mica surface. Now the thickness of the absorbed

protein layer on silicon and mica must be determined by AFM to corroborate these results.

3.4 Determination of Layer Thickness with AFM

Since mica is transparent with a refractive index near 1.6 [41] it would require a complex setup to use ellipsometry to measure the layer thickness of SELP on mica. Instead, we first measure the layer thickness of SELP–815K on silicon substrates using AFM and compare to the ellipsometry data and then measure the layer thickness on mica.

3.4.1 Methods

To determine the thickness of the protein layer on silicon, 5 scans at 300 to 400nN over a 250 nm by 250 nm area at 256 points and lines in contact mode to remove the SELP from the scanned area. The thickness of the layer was determined as the average depth of the engraving. Areas were sampled from the engraved areas to create histograms and fit with a single Gaussian to determine the average depth for each concentration of SELP–815K in same manner as determining the multilayer surface in the air images above. An average was chosen to better compare with ellipsometry data which relies on a model that assumes a uniform thin–film of protein on the silicon substrate.

To determine the minimum force necessary to engrave mica a control experiment was carried out using silicon tips (NSG01, NT-MDT) with a nominal spring

constant of 5 N/m. The actual spring constant was calculated via the thermal tuning method. At approximate forces of 50, 250, 500, and 750nN a 250 nm by 250 nm area was imaged at 512 points and lines in contact mode to attempt to remove mica layers. To determine the protein layer thickness on SELP–815K or 47K coated mica, a 250 nm by 250 nm area at 512 points and lines in contact mode were scanned at 200 nN normal force to remove the protein layer but not disturb the underlying mica surface.

The depth of the engraving on mica was determined by taking the average depth along 3 separate traces and then averaging the results. Each result was offset by the average height of the non–engraved portion of the mica which was determined to be 0.011 ± 0.019 nm for mica after first-order flattening. The RMS surface roughness for that mica, tip, and imaging conditions was found to be 0.24 nm and is shown as a dashed red line in Figure 3.5. The depth of the engraving for SELP was analyzed in a similar manner as for SELP coated silicon surfaces.

3.4.2 Results

Using AFM to remove the protein layer on silicon, as shown in Figure 3.4 show a layer thickness of 2.6 ± 0.8 nm for the 0.125 μg/mL SELP–815K and a layer thickness of 4.6 ± 0.7 nm for the 5 μg/mL SELP–815K sample on silicon which agree well with the values obtained from ellipsometry.
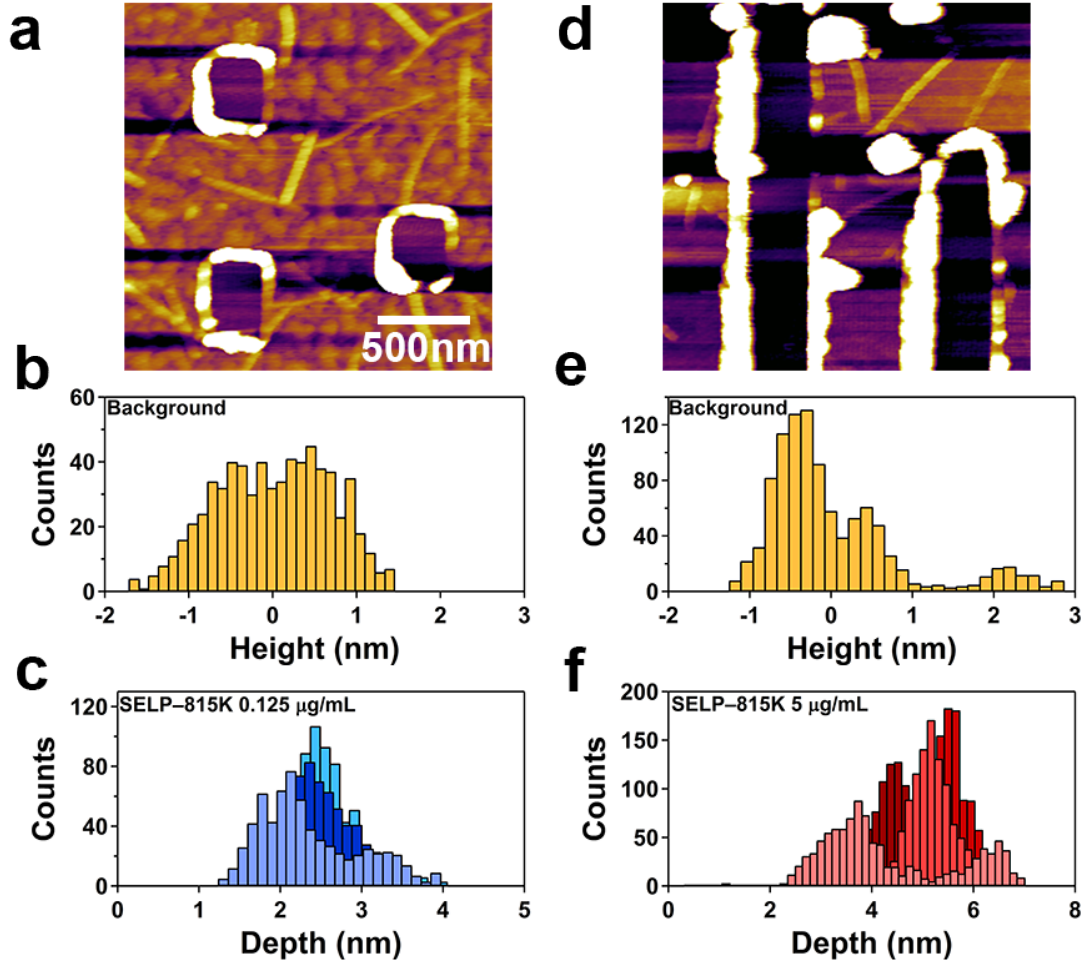
Figure 3.4: Determination of the SELP–815K layer thickness on silicon substrates. the engraving for a)0.125μg/mL and b)5μg/mL. The histograms of the background height (non–engraved area) are shown in b and e. The histograms for the engraving depths themselves are shown in c and f. The values determined for the layer thickness are found in the text.

Mica, unlike silicon, could be engraved using forces attainable by the NSG01 tips used therefore a control experiment show in Figure 3.5 with exact values shown in Table 3.1 determined that the no significant depth was engraved into mica for forces <250 nN. Therefore all layer determination for SELP–coated mica was done

at a force level of 200 nN to allow for deflection drift which would increase the applied normal force during engraving. The layer thicknesses for SELP–815K on mica are shown in Table 3.2. In cases where a bimodal distribution was obtained both layer thicknesses were reported. Initially, SELP layers were determined in air by engraving progressively larger areas with decreasing forces of 1500, 1000, 500, and 250 nN; however it was later determined through the control experiment just described that contact forces above 250 nN can damage the mica surface, therefore only layer thicknesses for the 250 nN force level are reported denoted in the table as "air".
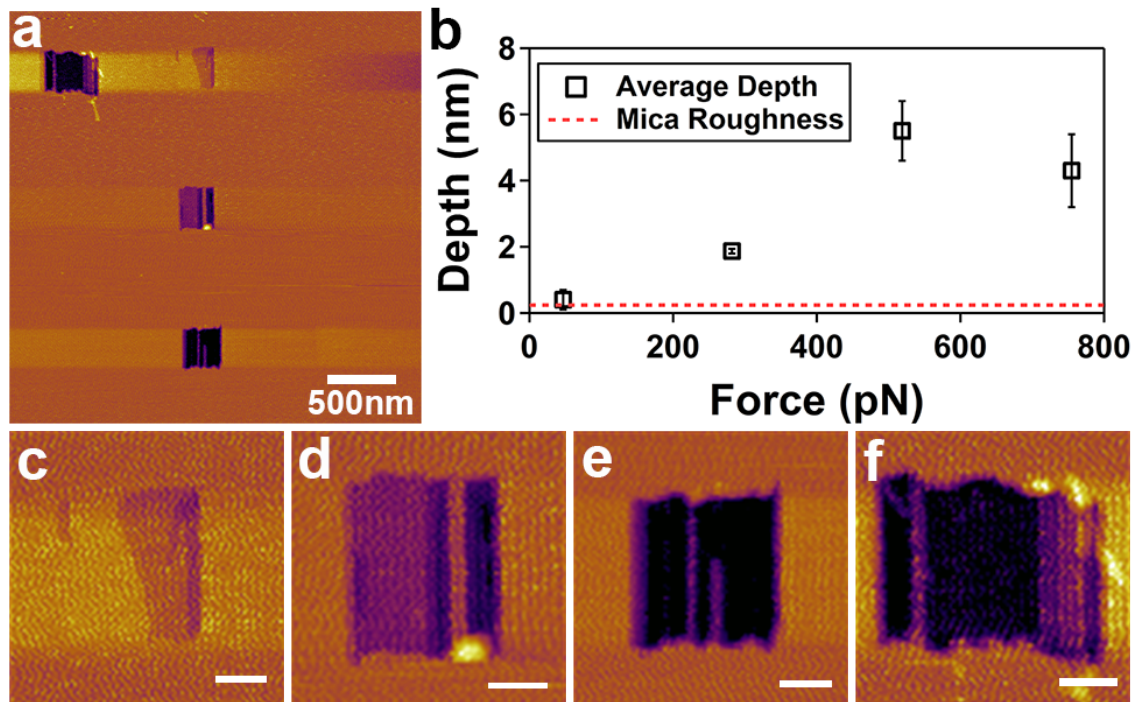
Figure 3.5: Determination of the minimum force needed to engrave a bare mica substrate. a) The entire 3μm by 3μm scan area. b)Plot of the depth of the engraving (black □). Error bars are standard deviations. The red dashed line shows the measured surface roughness for mica as a reference. For exact values, please refer to Table 3.1. c) 50 nN, d) 250 nN, e) 500 nN, and f) 750 nN engraves are expanded areas from (a). Scale bars in c-f are 100nm.

Table 3.1: Depth of Mica Engraving at Varying Force Levels

Force (nN)	Depth (nm)[a]	Significant[b]
47	0.4 ± 0.3	No
282	1.87 ± 0.07	Yes
519	5.5 ± 0.9	Yes
755	4.3 ± 1.1	Yes

[a] Average depth is corrected by mica reference height of 0.011 which is the average of three traces using sections of the trace in the nonengraved areas to adjust for the zero of height. Reported errors are standard deviations. [b] Significance is set at $p < 0.05$ as determined by Student's t-test comparing the average depth to the zero values of mica.

Table 3.2: AFM Layer Thickness on Mica in Water and Air

SELP	Condition	Concentration (μg/mL)	Depth (nm)[a]
815K	air	5	5.1 ± 0.9
		0.125	1.4 ± 0.7
	water	5	2.2 ± 0.4 and 1.3 ± 0.3
		0.250	2.0 ± 0.3 and 1.1 ± 0.3
		0.125	2.1 ± 0.4 and 1.3 ± 0.5
47K	water	40	1.9 ± 0.4
		4	1.0 ± 0.5
		0.4	1.0 ± 0.5

[a] Average depth is corrected by height of surrounding area. Errors are standard deviations.
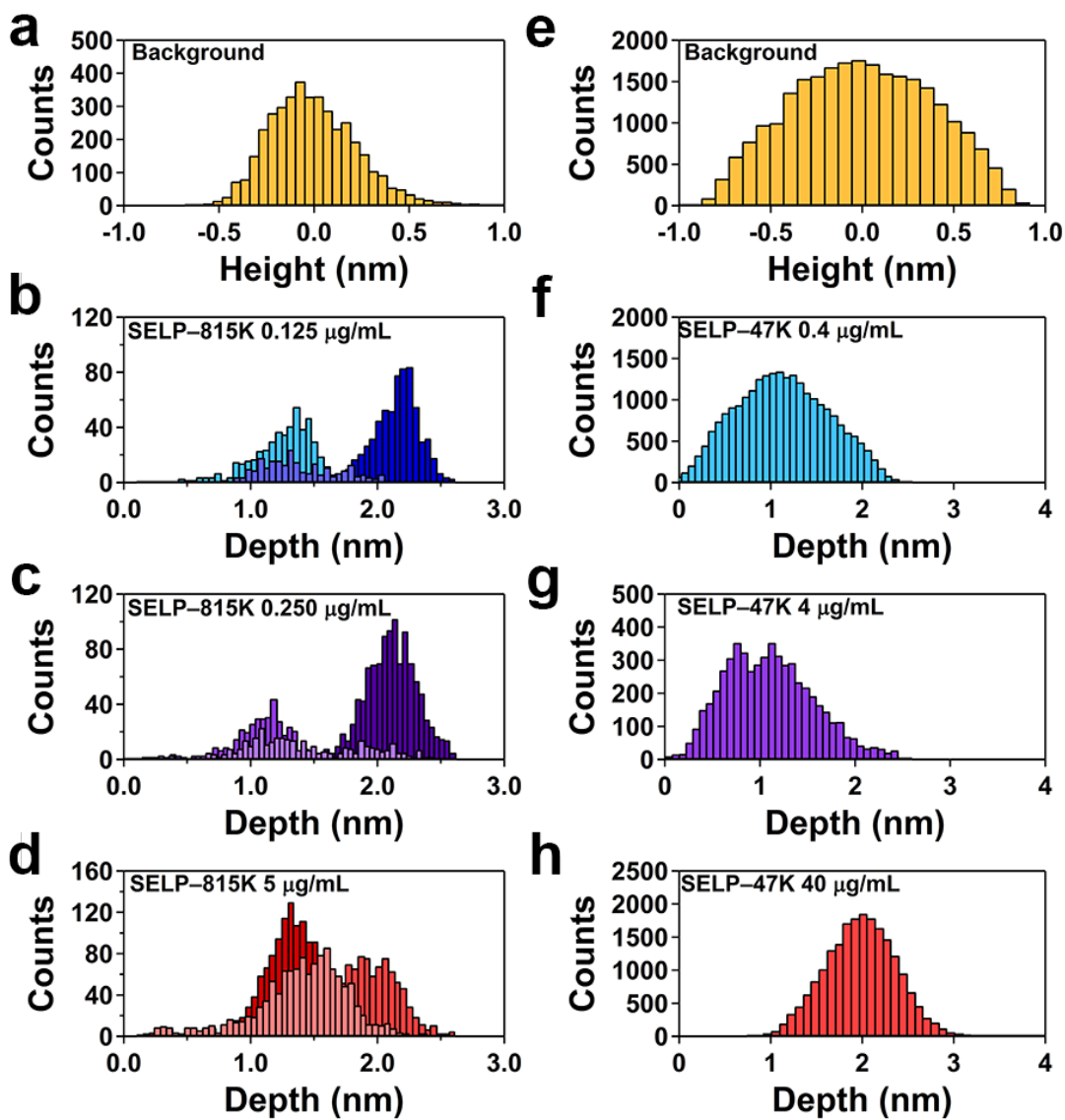
Figure 3.6: Representative distributions of layer thickness for SELP–815K and 47K in water at various concentrations. a) Background distribution for 815K shows average height outside of the engraving is 0 nm. b) 0.125, c) 0.250, and d) 5 μg/mL SELP–815K shows 2, 1 nm layers that are both present at all concentrations depending on the area measured. e) SELP–47K background is also 0 nm. f) 0.4, g) 4, and h) 40 μg/mL SELP–47K do not show two distinct layers although the thicknesses are similar. The shades indicate different areas measured. Only one of the histograms is shown for 47K as all areas measured show a similar distribution.

3.4.3 Discussion

The multilayer structure of SELP–815K on silicon does not show the multilayer surface as it does on mica as can be seen in the air images. Removing individual layers of SELP from the mica surface is difficult, but different concentrations of SELP–47K and 815K do show a difference in layer thickness when both have the protein layer removed at the 200 nN force level. Both silicon and mica in air, when engraved show a layer thickness of about 4 nm for 5 μg/mL SELP–815K in agreement with the ellipsometry data.

Interestingly, in water for 815K, the layer thickness shows a bimodal distribution of depths for the engravings which shift in the populations of 1nm and 2 nm depths to a layer of intermediate average depth as the concentration of the SELP increases from 0.125 to 0.250 to 5 μg/mL. This could indicate the bottom-up assembly of a bilayer of SELP with the elastin-like portions oriented towards the mica as the positively charged lysine should associate with the negatively charged surface and the silk-like portions holding the bilayer together where the bimodal distributions show areas where the bilayer is formed and those that are not. The slight decrease in the average thickness for the highest concentration of 815K maybe be due to rearrangement of SELP within the layer as it absorbs onto the mica. This construct would also explain why a 20–fold increase in concentration causes no further increase in layer thickness as the surface may be resistant to further addition of SELP to form higher multilayer structures. SELP–47K shows similar layer depths over a large range of concentrations as well and its surface structure may be similar

to 815K although thickness and structure are by no means the same.

This interpretation of this multilayer structure must be reconciled with the heights of fibers formed from 815K and 47K. 815K fibers show heights of 3.5 ± 0.7, 6.6 ± 0.8, and 8.2 ± 1.4 nm (n = 66 fibers) in water and 2.8 ± 0.4 and 4.6 ± 0.5 nm (n = 5) in air. 47K fibers show heights of 2.6 ± 0.6 and 5.2 ± 0.8 nm (n = 39) in water and 1.5 ± 0.4, 3.1 ± 0.6, 4.6 ± 0.8, and 6.9 ± 0.6 nm (n = 13) in air. These fibers likely push out from the the top–most layer as do the nanodots with some variation in height owing itself to the structure starting directly on the mica versus being entirely on top of the two layers to being located in the plane of the silk units within the two layer structure. A schematic of the possible surface structure is shown in Figure 3.7. Height differences in the fibers between water and air could also be the result of dehydrating the structure, resulting is lower heights or fixing the elastin portions of the protein which likely forms some of the diffuse mobile layer in water and is invisible to imaging, which would be result in higher observed heights.
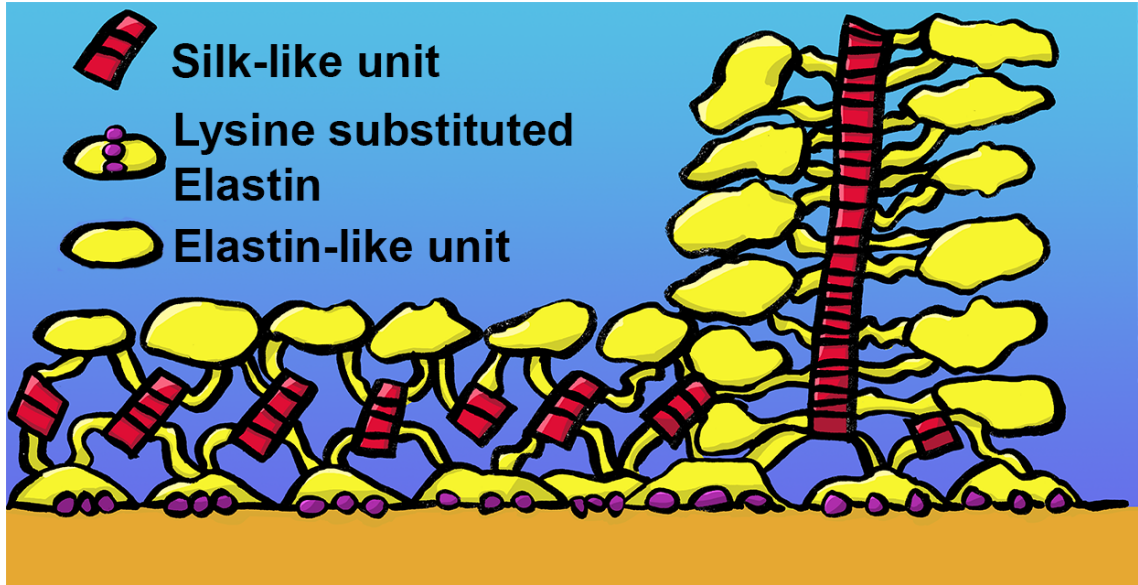
Figure 3.7: Schematic drawing of the proposed SELP structure on mica in water showing how fibers may be situated in that structure. Mica is shown in brown and the blue background represents the aqueous environment. Elastin units are shown in yellow, silk units in red and the lysine in the lysine–substituted elastin in purple which should be electrostatically bound to the mica surface.

The layers could be thicker in air for 815K due to several reasons, one is that frictional force is in higher in air and thus the 250 nN setpoint may have removed some of the mica surface which could add an additional nanometer to the measured depth if that is the case. No mica surface may have been removed, but mearly some of the SELP layer which adhered tighter to the mica surface may have come off under the additional force. The packing of SELP into a layer in air and water are likely different and the packing in air could be influenced by the relative humidity which was not controlled with our setup. The air images of SELP–815K show the lowest resolvable layer as appearing to have some symmetry opening the possibility

that the lower layer of SELP is epitaxially ordered and that the layer in or on which the fibers and nanodots grow must be adhered to this layer. Perhaps the lattice matching is only favored once the sample is dehydrated and this behavior or the initial lattice-matched layer is just obscured in liquid due to more surface diffusion and the more mobile protein coupled with its large size is not able to order with the mica lattice until the sample is dried. If this is the case then the layers formed by SELP in air may have differences in depth due to a different surface organization.

3.5   SEM of AFM tips

Characterization of the AFM tip is important in order to asses the tip surface under various treatments in an effort to better understand how the SELP is absorbing to tip surface; however, doing so poses several problems. Obviously, imaging the tip surface with AFM is not feasible and non-conductivity of the silicon nitride composition of the tips makes SEM difficult. If a large enough change in the tip radius were to occur after the coating procedure, then that increase could be observed with SEM. The caveat here is that the large tip radius variation as stated by the manufacture of 20–60 nm as well as ellipsometry results of SELP absorbed onto silicon forms a layer <5 nm thick then changes in the radii may not be observable. To mitigate these issues we can attempt to correlate the measure tip radii with adhesive or pull–off force to better understand the differences in tips that patterned different features on various substrates.

3.5.1 Methods

Silicon nitride (MLCT, Bruker) AFM tips were mounted to an aluminium 90° SEM sample mount with carbon tape. Images were obtained on a Hitachi SU-70 SEM at a typical working distance of 5.8 nm and 10 keV accelerating voltage. Tip radii were determined from SEM images using ImageJ software by drawing a circle approximating the curvature of tip and circles were drawn five times on each image to minimize errors in the method. From the area of the circle drawn, the radius is easily obtained.

3.5.2 Results

Figure 3.8 shows the SEM images of silicon nitride AFM tips that produced differences in patterning and force behavior for SELP–47K. As can be seen in Table 3.3 the average tip radius for all conditions was approximately 50 nm. This implies that either the SEM determination is not sensitive enough given the non–conductivity of silicon nitride which results in poor SEM contrast due to charging effects and the expected thickness of SELP layer would only increase the radius by a few nm which may not be detectable as the tips themselves vary from 30 to 70 nm in radius. Therefore, the SEM can give us the average tip radii and verify that it falls within the manufacture specified range; however, minor differences arising due to the various coating methods are not possible to detect with SEM.
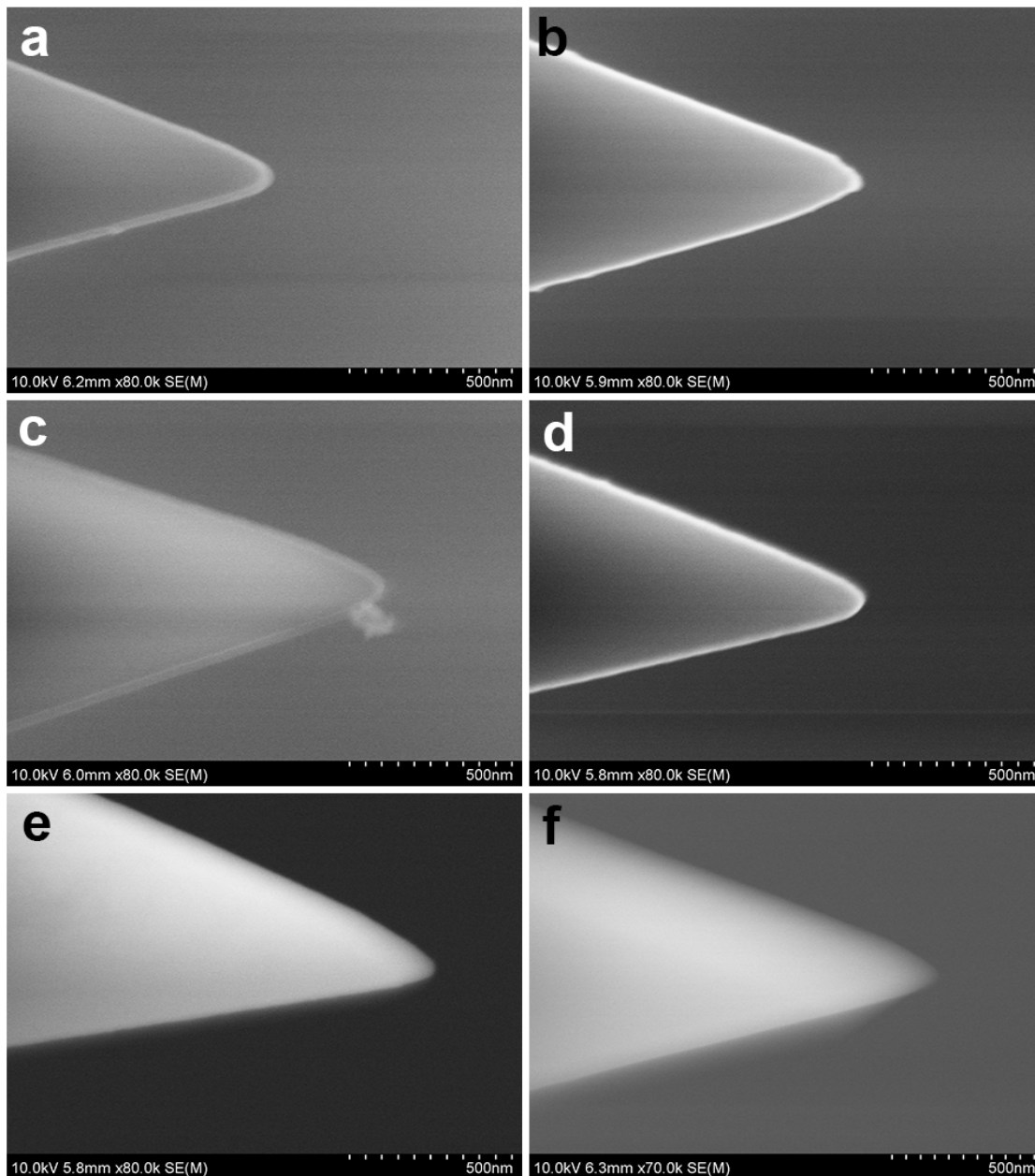
Figure 3.8: SEM images of SELP–47K–coated AFM tips used that created a) no features, b) nanodots on mica, c) fibers on mica. SEM images of the various tip preparation methods d) UV/Ozone cleaned uncoated, e) coated and dried in a Veeco gel box, and f)coated and dried in a polystyrene petri dish.

Table 3.3: Tip radii from SEM for different tip preparation conditions

Tip Preparation[a]	Substrate	Drying Time (h)[e]	Features	Radius (nm)[f]
10μL of SELP[b]	mica	3	fibers	66.1 $\pm$ 2.1
10μL of SELP[b]	mica	3	fibers	34.2 $\pm$ 0.6
10μL of SELP[b]	mica	12–16	no features	52.9 $\pm$ 1.0
10μL of SELP[b]	mica	3	fibers	54.7 $\pm$ 1.6
70μL of SELP[c]	mica	12–16	no features	55.8 $\pm$ 1.9
20μL of SELP[d]	mica	0.5 (vac)	fibers/nanodots[g]	56.2 $\pm$ 2.4
20μL of SELP[d]	mica	1 (vac)	fibers	43 $\pm$ 3
Cleaned only[a]	mica/SELP	—	nanodots[h]	67 $\pm$ 6
Cleaned only[a]	mica/SELP	—	fibers[i]	63.6 $\pm$ 1.5
20 μL of SELP[d]	mica/SELP	1 (vac)	nanodots	40 $\pm$ 3

[a] Cleaned refers to 15 min UV/Ozone cleaned and uncoated, all tips were cleaned in this manner. [b] prepared in a Veeco gel box [c] prepared in a piranha–cleaned glass beaker. [d] prepared in a polystyrene petri dish [e] samples were dried under ambient conditions unless specified by (vac) meaning that the sample was dried under vacuum [f] All errors are standard deviations of five measurements as discussed in the text. [g] Scanning produced fibers and force curves produced nanodots [h] nanodots only on 0.04 μg/mL SELP-47K [i] fibers only on 0.4 μg/mL SELP-47K

3.6 Discussion

The results of the tip characterization show that all of the tips, regardless of treatment, appear to have a very similar tip radius. The large variation of tip radii as per manufacturer specification relative to the expected film thickness based

on ellipsometry data coupled with the poor resolution of SEM on non–conductive silicon nitride tip surfaces is the most likely cause. This may have been averted somewhat by imaging the same tip before and after the coating procedure; however, tips imaged with SEM were sometimes not usable afterwards, possibly due to being coated with carbon from the carbon tape during the imaging process.

The coated tips that were measured were also used for patterning before taking a SEM image in an effort to correlate tip radius to patterned features so it is also possible that material that had absorbed onto the tip came off during the patterning process and may have even depleted the tip surface back to its original state as the SELP was merely dried to the tip and not covalently attached.

Chapter 4:   Differentiation of Nanodots with Force Spectroscopy

4.1   Introduction

Because the morphology of nanodots is difficult to assess due to both potential tip artifacts as well as the instability of the nanopatterns themselves, we must look to the force curves used to generate the nanodots in order to differentiate between those that are capable of nucleating fiber growth and those that are not.

Single–Molecule Force Spectroscopy (SMFS) or Dynamic Force Spectroscopy (DFS) can be used to understand the energy landscape of self-assembly by looking at the case of dimerization. However, with SELP that readily assembles in the presence of a surface the ability to stretch a single–molecule is not trivial and would likely require covalent attachment to achieve. This poses a problem as the stretching of an unknown number of molecules can convolute the force spectra along with the lack of detailed structural information with which to interpret the spectra, making quantitative information difficult or impossible to obtain.

We can however look at the force curves qualitatively by comparing the presence of tethering behavior (described below) in relation to the both the ability of those curves to form nanodots as well as whether those nanodots are capable of forming fibers spontaneously, under mechanical stimulus, or not a all.

In addition to qualitatively observing tethering behavior we can fit stretching that is observed with the Worm–Like–Chain (WLC) model to obtain contour lengths for individual rupture events and compare the peak–to–peak distance to the silk or elastin portions in order to obtain some mechanistic insight as to which portions of the molecule are being stretched during the tethering behavior. To obtain peak–to–peak histograms, curves were fit with the WLC model using Igor software and then successive contour lengths binned ignoring any contour lengths over 100 nm as the molecule cannot physically be stretching further than 100 nm with a 100 nm force distance. Contours above that value are likely the result of a poor fit to the WLC model as is excluded from the analysis. Histograms were fit with 1 or 2 Gaussian curves and reported values are the mean and standard deviation from that fitting. In order to obtain sufficient distances all coated tips on bare mica and all bare tips on SELP–47K surfaces were pooled. Based on sequence, SELP–47K should show lengths of 3.8, 12.2, and 7.6 nm for the silk–like blocks and 15.2 nm for the elastin–like blocks calculated by assuming a contour of 0.38 nm per amino acid.

The methods for obtaining the results that follow were previously described in Section 2.2. Briefly, we used a continuous force mode in an attempt to create nano–sized deposits of protein with uncoated and SELP coated silicon nitride AFM tips on both bare mica and SELP coated mica starting with a control experiment in which bare tips were used on a bare mica surface. SELP–47K was used as 815K tended to pattern fibers non–specifically on the mica surface making the images difficult to interpret.

4.2 Results

4.2.1 Bare Tips on Bare Mica Control

Bare tips used on freshly cleaved mica produced no stretching events and did not result in the formation of features on the mica surface as shown in Figure 4.1a and addition of 1M NaCl caused the repulsive force in the approach portion of the curve to disappear as can be seen in Figure 4.1d and e which indicates that this repulsion is electrostatic in nature as a result of the negatively charged mica [42] surface and the slightly negatively charged SiO_2 tip surface in water [43]. After washing the sample back into water to remove the salt solution, the repulsive region remains absent likely due to salt absorbing on the mica and/or tip and neutralizing the surface. The salt and possibly other debris can be seen in Figure 4.1c showing that the salt is likely absorbing onto the mica surface.
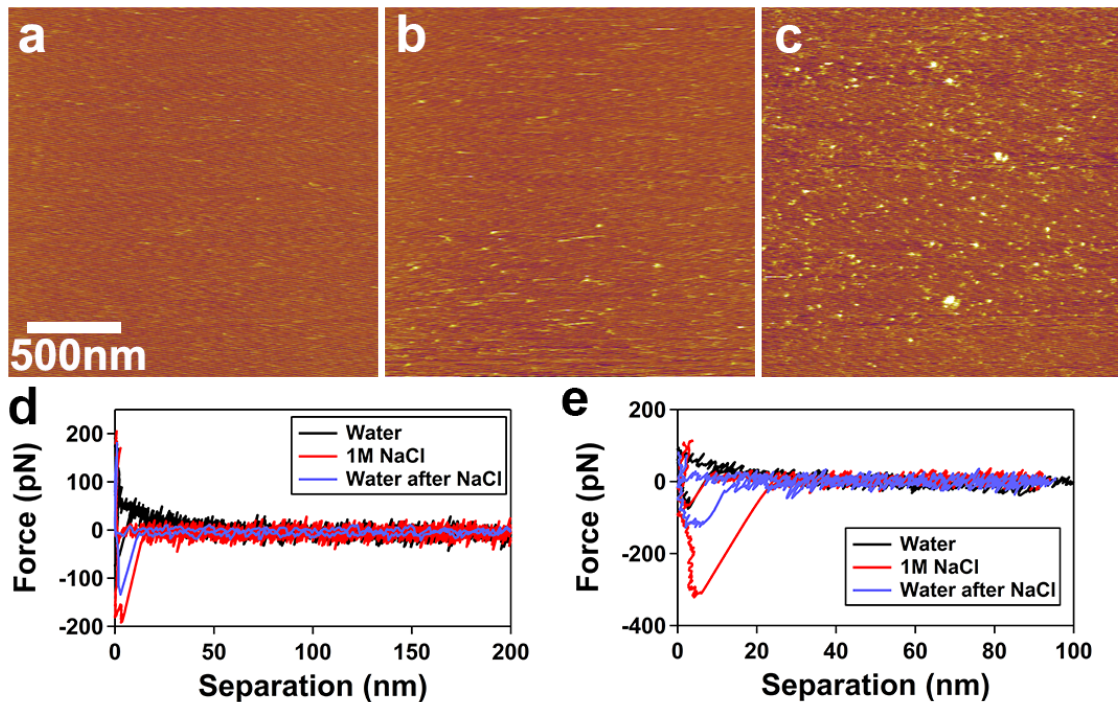
Figure 4.1: a) Bare mica surface imaged with a bare tip. b) Mica surface in 1M NaCl c)After washing the sample back into water. Representative continuous mode force curves for each condition with 100pN trigger and 2s dwell times at d) 1000nm and e) 100nm force distances.

4.2.2 Tethering Behavior

At 100nm retraction distances, a particular force curve is seen in nearly all instances of nanodot creation at this force distance. We are calling this behavior "tethering" as we are interpreting the repulsive force on approach as compression of the molecule against the mica surface. This force behavior can be seen in Figure 4.2. Although, observation of this behavior did not guarantee the creation of nanodot, this force behavior could be seen for those sets of curves that did result in nanodot formations with few exceptions. These exceptions could be due larger force distances

in which tethering was not possible without tip or surface detachment of the SELP, indicating the certain nanodots may be formed with a single force curve as is the case for Figure 2.2b in which a single force curve generates an array of nanodots on an SELP–815K coated surface.
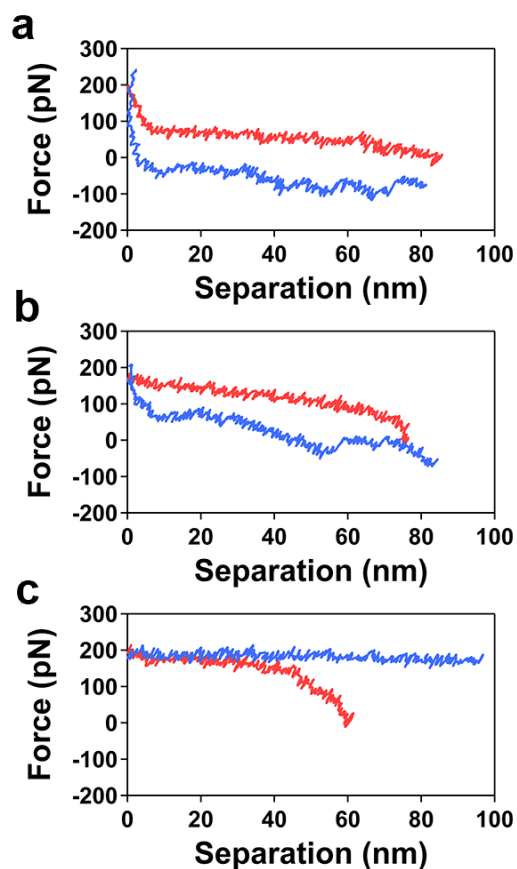

Figure 4.2: Force curves representative of tethering behavior. The curves shown are sequential curves taken in continuous pulling mode and show the repulsive approach portion in (a) which is repeated in curves (b) and (c) as the molecule is still attached between the tip and surface for those curves. Red curves are approach and blue are retraction.

4.2.3 Bare Tips on SELP–47K Substrates

Bare (UV/Ozone-cleaned and uncoated) tips used on SELP–47K surface are also able to create nanodots which are able to result in localized nucleation. As can be seen in Figure 2.5 a nanodot produced on this substrate was able to be laterally stretched which resulted in the growth a nanofiber from the nucleation location patterned via the continuous force mode method. The force curves used to create this nanodot showed the tethering behavior in 38% of the force curves.

The peak–to–peak distances, as shown in Figure 4.3 for bare tips on SELP–47K surfaces show two distances of 22 ± 3 and 48 ± 2 nm. Neither length corresponds to an individual silk or elastin block and could be the result of several combinations of these blocks.
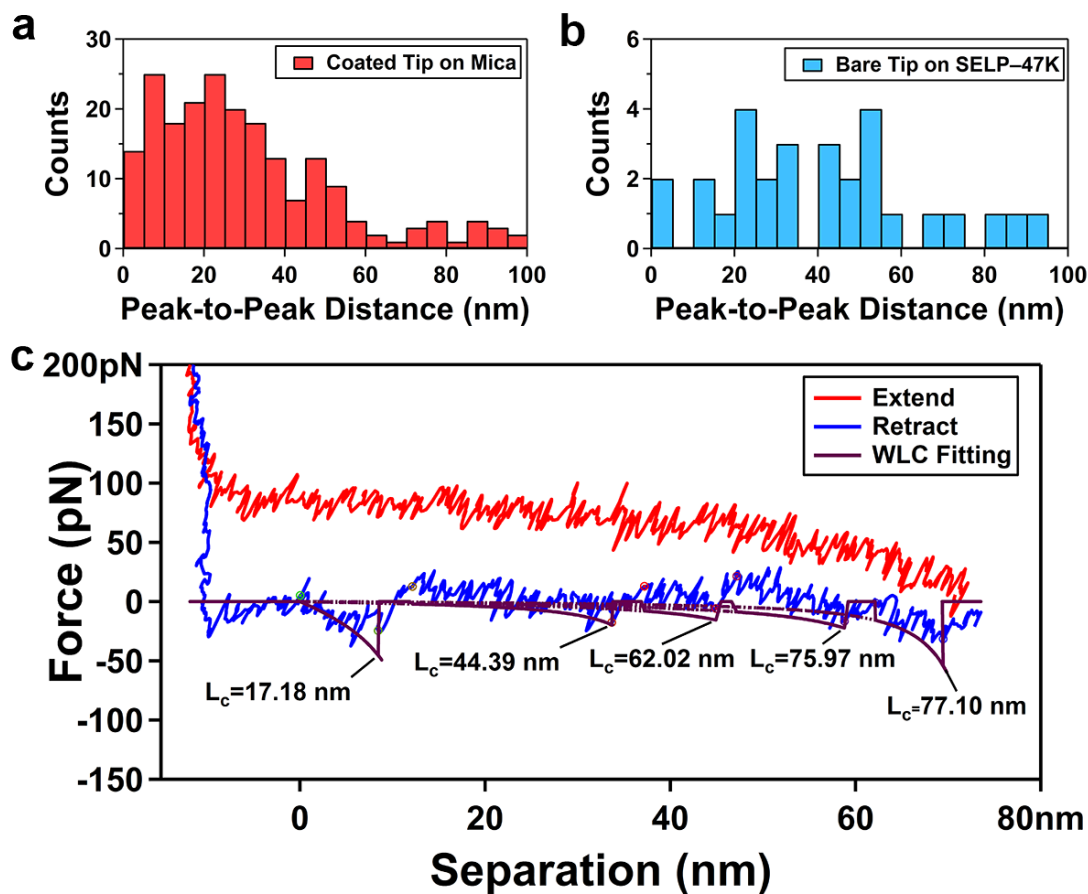
Figure 4.3: Peak–to–peak distance histograms for a) SELP coated tips on bare mica surfaces and b) bare tips on SELP–47 substrates. c) Example of the WLC fitting showing two peak–to–peak distances of 17.63 and 13.95 nm respectively going from 44.39 nm to 62.02 nm to 75.97 nm contour lengths.

4.2.4 Coated Tips on Bare Mica Substrates

Nanodots created on a bare mica surface using a coated tip can be see in Figure 2.4 in Chapter 2. Using a coated tip on bare mica to take 10 curves at each of nine points at a 200 pN trigger, 100 nm retraction distance, and 5 second dwell time, a single nanodot was created which can be seen to have a fiber growing

from it perpendicular to the scanning direction as can be seen in Figure 4.4. The orientation suggests that the fiber was mechanically induced through the tapping mode scanning of the surface to verify the patterning of the nanodots.

The peak–to–peak distance shown in Figure 4.3 for coated tips on a bare mica surface shows a distance of 15 ± 4 nm which corresponds to either 2 or 4 silk blocks or 1 elastin block. This can be interpreted as either the silk blocks remaining together and only the elastin portion of the curve being stretched or it could be pulling multiples of silk blocks apart in the course of the stretching. Breaking and reforming silk–like portions of SELP during continuous pulling may be allowing the alignment of the silk blocks during the tethering which potentially creates a nucleation site.
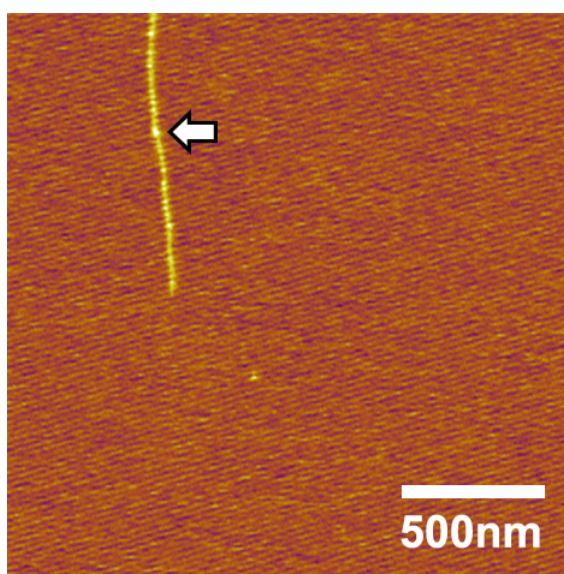

Figure 4.4: Using a SELP–coated tip on bare mica, a single nanodot (indicated by the white arrow) was created resulting in the formation of fiber growth perpendicular to the scanning direction.

4.2.5 Coated Tips on Dried and Re-hydrated SELP-47K Substrates

Some SELP-47K substrates were dried and re–hydrated in an effort to mimic dried nature of the SELP on the tip surface and force curves were taken using both coated and uncoated tips. The force behavior for these samples also showed tethering in 30% of the force curves taken at 100 nm force distance and all sets of curves created nanodots which did not form into fibers.

Table 4.1: Tethering Force Behavior in Relation to the Types of Nanodots

Tip	Concentration (μg/mL)^a	Nanodots	Fibers Formed^a	Tethering Curves (%)
bare	0.4 μg/mL^d	Yes	No	30%
bare	0.04 μg/mL	Yes	No	0%
bare	0.04 μg/mL	Yes	Yes	38%
coated	mica	No	No	12%
coated	mica	Yes	Yes	0%
coated	mica	No^b	—	60%
coated	mica	Yes	Yes	83%

^{a} Fibers formed indicates that fibers were formed from the nanodots themselves not that only fibers appeared after patterning. ^{b} Only fibers were observed after taking force curves. ^{c} Formed a single fiber with directional control as shown in Figure 4.4 ^{d} Sample was air dried and Re–hydrated before taking force curves. ^{e} Fiber formed after lateral stretching of the nanodot.

4.3 Discussion

The creation of nanodots using the methods described lends itself to no small amount of experimental variation. This is due in part to variation in tip radii and/or coating of the tip with SELP. The local surface concentration of SELP likely plays a large role as well; however, based on the layer thickness data, that surface is roughly the same thickness over a broad range of concentrations although that in no way is meant to imply that the structure of those surfaces and the orientation of the SELP within them is the same. Further studies are needed to characterize the fine structure of SELP at the mica surface in order to answer that question.

Table 4.1 shows the percentage of curves that showed the tethering behavior described above along with whether a coated or uncoated tip was used and the what type of nanodots were formed with that surface/tip combination. The single nanofiber was part of set of curves in which 83% of the curves taken at 100 nm force distance showed tethering. The nanodots formed in which tethering behavior was not present did not grow into fibers during the time course of the experiment. It is thought that the tethering force behavior's repeated compression and extension of the SELP molecules creates conditions under which the silk blocks of the SELP can align in a similar manner to tapping mode and contact mode mechanical stimulus. It may only require a single stretch to perform this alignment as certain sets of force curves can produce nanodots even at 1000 nm retraction distances which is three times the theoretical contour length of SELP–47K making tethering unlikely as stretching at that distance will result in detachment either from the mica surface

or from the AFM tip. Nanodots can also be created without tethering as is the case for Figure 2.4 in which two of the six nanodots formed remain after initially scanning the area and one of which spontaneously grows into nanofibers due to the lack of directional control present. An alternative explanation for this behavior is that the nanodot formed is merely encapsulated by the fiber growth which resulted from the tapping mode stimulus during the imaging. The nanodot itself did not grow into fibers, which means that all cases of nanodots forming fibers show at least 30% of curves with tethering making the presence of tethering necessary, but not sufficient for the nanodot to act as a nucleation site.

The peak–to–peak distances show distances for bare tips on SELP–47K surfaces that do not directly correspond to the theoretical contour lengths of individual silk or elastin blocks whereas coated tips on mica showed a distance of 15 nm which is the distance of 2 or 4 silk blocks or 1 elastin block. In the first case the lack of correlation could either a lack of data for a pattern to emerge or the result of a different structure of nanodots formed in those cases which are less likely to nucleate into fibers indicating that those nanodots are a thermodynamically stable amorphous aggregate that cannot further rearrange into a fiber–competent confirmation as a large amount mechanical stimulus may be necessary and would likely result in the nanodot being swept away rather than growing into a fiber. In the case of the bare tips on mica, fibers appear to nucleate spontaneously from nanodots or under the mechanical force of tapping mode rather than necessitating lateral stretching. This indicates that energy barrier for these nanodots to grow into fibers may be lower than nanodots that are likely closer to stable amorphous aggregates which may be

due to alignment of the silk blocks during the continuous force curve acquisition.

There appears to be, overall, two classes of nanodots: those that can be formed with a single force curve and those that appear to require the repetitive pulling present in the tethering behavior. Whether or not the nanodots grow spontaneously into fibers without directional control or whether they require further mechanical stimulus to align and grow with directional control may be linked to these two distinct ways of creating the nanodots. At this time however, there are not enough nanodots which have been created that are capable of nucleating fiber growth to separate these two populations rigorously.

Chapter 5:   Conclusions and Future Directions

5.1   Directional Control of Fibers from Localized Nucleation

Previously, we have determined that SELP grows perpendicular to the scanning direction and using that we have created both microscale patterns of aligned fibers [31] and single nanofibers [32]. However, the nucleation location was found randomly within the scan line with smaller scan areas decreasing the nucleation probability. Using a continuous force mode, we are able to nucleate SELP fibers within a 50 nm area; however, there is a low probability of success as well as poor directional control as the nanodots created via this method appear to be heterogeneous in both their stability as well as whether mechanical force causes them to grow into nanofibers if they are able to at all.

5.2   Future Directions of Mechanically Induced Self-assembly

The main issue with the continuous force method to create a nucleation site for SELP fibers is the inability at this time to accurately predict the exact conditions for creating a nanodot that neither lies dormant under mechanical stimulus nor grows seemingly spontaneously into a fiber. Ideally, one should be able to create

a nanodot that only under mechanical stimulus (tapping or lateral force) will grow into a fiber as the stretching of the SELP during this mechanical stimulus is likely responsible for the alignment of the β–strands in the silk–like regions thought to be the main composition of the fibers.

It is likely a very small window of conditions that would even allow for the creation of such a nanodot; however, if they could be reliably created in such a manner that window will likely be found using either SELP coated mica at a concentration below that which forms fibers and then adding additional SELP to the formed nanodots to allow for fiber growth. The difficulty with this is that the created nanodots are not always stable and it is therefore sometimes impractical to image the same area of the mica surface over the course of several days or weeks. Even using high force to create a reference mark on the mica surface, the nanodots themselves may dissipate or diffuse during that time. Some can even be swept away in a single scan in contact mode.

5.3 Outstanding Questions about SELP

There are several questions that still remain for SELP self-assembly on mica which are mainly to do with the structural characterization of the SELP coated mica surface. The surface in air showed a bilayer structure where the surface layer appeared to have symmetry which could indicate its epitaxial alignment to the mica which could tested by obtaining additional images of the surface under both water and air at varying concentrations of protein to attempt to observe the bottom layer

in sufficient detail to verify the symmetry. Dehydrating the surface rapidly with a non–solvent for SELP, such as methanol may also change the layering of SELP. The surface structure should be assessed using a complimentary technique such as IR or Raman spectroscopy to determine the β–sheet content of the SELP under the various conditions.

One possible route to a monolayer of SELP is to functionalize a gold surface with an Nitrilotriacetic acid (NTA)–terminated alkanethiol and then treat the surface with $NiCl_2$ so that the His–tag of the SELP would chelate the Ni^{2+} along with the NTA. The caveat here is the SELP could still likely self-associate and form a bilayer mediated by the silk blocks as discussed in Section 3.4.3. If a monolayer could be formed then the dimerization reaction could be further investigated using SMFS for both the monolayer and bilayer constructions to obtain more information about the tip surface interactions with coated and uncoated tips on SELP and mica coated surfaces that are convoluted by the presence of multiple molecules.

A better understanding of forces involved as well as the surface structure may provide the missing pieces which would allow a more reliable creation of nanodots which are able to grow into fibers so that effect of mechanical force can be studied more easily as well as to provide the ability to study if directional control is possible when nucleation sites are created in this manner.

5.4 Role of Nanodots in Amyloidogenesis

The heterogeneity of the created nanodots mirrors that of other amyloidogenic systems which are thought to contain a variety of pre-fibular aggregates with varying degrees of stability and ability to form filaments. If the issues discussed in the previous section could be resolved, then SELP could be used as model system to understand other amyloids as the timescale of the self-assembly is much shorter which can allow for the direct observation of fiber growth. If nanodots of another protein, such as Tau, were to be created in this manner, then it may be possible nucleate fibers *in situ* with an AFM tip, which, to our knowledge as never been accomplished. The ability to reproducibly create nanodots of Tau could aid in the development of drugs which either promote or inhibit the evolution of Tau oligomers into fibers by being able to create a large population of oligomeric structures at the surface to study their growth into fibers.

5.5 Implications for Peptide Based Self-assembly

As SELP is biocompatable, there is potential use for the creation of amy-loid–based materials using SELP. SELP has already been shown to provide an an optically transparent film [10] that can support human fibroblast cells [12]. The ability to gain finer control of self-assembly may open up new applications for this protein especially if an optimized continuous force mode technique could be scaled to arrays of hundreds or thousands of tips as has been done for PPL [44].

Bibliography

[1] R. Nelson, M. R. Sawaya, M. Balbirnie, A. O. Madsen, C. Riekel, R. Grothe, and D. Eisenberg. Structure of the cross-beta spine of amyloid-like fibrils. *Nature*, 435(7043):773–778, 2005.

[2] L. Pauling, R. B. Corey, and H. R. Branson. The structure of proteins - 2 hydrogen-bonded helical configurations of the polypeptide chain. *Proceedings of the National Academy of Sciences of the United States of America*, 37(4):205–211, 1951.

[3] L. Pauling and R. B. Corey. 2 rippled-sheet configurations of polypeptide chains, and a note about the pleated sheets. *Proceedings of the National Academy of Sciences of the United States of America*, 39(4):253–256, 1953.

[4] F Ulrich Hartl and Manajit Hayer-Hartl. Converging concepts of protein folding in vitro and in vivo. *Nature structural & molecular biology*, 16(6):574–581, 2009.

[5] H. A. Lashuel and P. T. Lansbury. Are amyloid diseases caused by protein aggregates that mimic bacterial pore-forming toxins? *Quarterly Reviews of Biophysics*, 39(2):167–201, 2006.

[6] D. M. Fowler, A. V. Koulov, W. E. Balch, and J. W. Kelly. Functional amyloid - from bacteria to humans. *Trends in Biochemical Sciences*, 32(5):217–224, 2007.

[7] C. A.E. Hauser, S. Maurer-Stroh, and I.C. Martins. Amyloid-based nanosensors and nanodevices. *Chemical Society Reviews*, 43(15):5326–5345, 2014.

[8] D. M. Fowler, A. V. Koulov, C. Alory-Jost, M. S. Marks, W. E. Balch, and J. W. Kelly. Functional amyloid formation within mammalian tissue. *Plos Biology*, 4(1):100–107, 2006.

[9] Samir K. Maji, Marilyn H. Perrin, Michael R. Sawaya, Sebastian Jessberger, Krishna Vadodaria, Robert A. Rissman, Praful S. Singru, K. Peter R. Nilsson, Rozalyn Simon, David Schubert, David Eisenberg, Jean Rivier, Paul

Sawchenko, Wylie Vale, and Roland Riek. Functional amyloids as natural storage of peptide hormones in pituitary secretory granules. *Science*, 325(5938):328–332, 2009.

[10] W. B. Teng, J. Cappello, and X. Y. Wu. Physical crosslinking modulates sustained drug release from recombinant silk-elastinlike protein polymer for ophthalmic applications. *Journal of Controlled Release*, 156(2):186–194, 2011.

[11] R. Dandu, A. Von Cresce, R. Briber, P. Dowell, J. Cappello, and H. Ghandehari. Silk-elastinlike protein polymer hydrogels: Influence of monomer sequence on physicochemical properties. *Polymer*, 50(2):366–374, 2009.

[12] Raul Machado, André Da Costa, Vitor Sencadas, Carmen Garcia-Arévalo, Carlos M Costa, Jorge Padrão, Andreia Gomes, Senentxu Lanceros-Méndez, José Carlos Rodríguez-Cabello, and Margarida Casal. Electrospun silk-elastinlike fibre mats for tissue engineering applications. *Biomedical Materials*, 8(6):065009, 2013.

[13] J. Cappello, J. W. Crissman, M. Crissman, F. A. Ferrari, G. Textor, O. Wallis, J. R. Whitledge, X. Zhou, D. Burman, L. Aukerman, and E. R. Stedronsky. In-situ self-assembling protein polymer gel systems for administration, delivery, and release of drugs. *Journal of Controlled Release*, 53(1-3):105–117, 1998.

[14] W. B. Teng, Y. D. Huang, J. Cappello, and X. Y. Wu. Optically transparent recombinant silk-elastinlike protein polymer films. *Journal of Physical Chemistry B*, 115(7):1608–1615, 2011.

[15] J. E. Gillam and C. E. MacPhee. Modelling amyloid fibril formation kinetics: mechanisms of nucleation and growth. *Journal of Physics-Condensed Matter*, 25(37), 2013.

[16] Elias Akoury, Michal Gajda, Marcus Pickhardt, Jacek Biernat, Pornsuwan Soraya, Christian Griesinger, Eckhard Mandelkow, and Markus Zweckstetter. Inhibition of tau filament formation by conformational modulation. *Journal of the American Chemical Society*, 135(7):2853–2862, 2013.

[17] Alejandro Barrantes, Javier Sotres, Mercedes Hernando-Perez, Maria J Benitez, Pedro J de Pablo, Arturo M Baro, Jesus Avila, and Juan S Jimenez. Tau aggregation followed by atomic force microscopy and surface plasmon resonance, and single molecule tau-tau interaction probed by atomic force spectroscopy. *Journal of Alzheimer's Disease*, 18(1):141, 2009.

[18] Wonseok Hwang, Bo-Hyun Kim, Ramesh Dandu, Joseph Cappello, Hamidreza Ghandehari, and Joonil Seog. Surface induced nanofiber growth by self-assembly of a silk-elastin-like protein polymer. *Langmuir*, 25(21):12682–12686, 2009.

[19] A. S. Lea, A. Pungor, V. Hlady, J. D. Andrade, J. N. Herron, and E. W. Voss. Manipulation of proteins on mica by atomic force microscopy. *Langmuir*, 8(1):68–73, 1992.

[20] F. Macchi, S. V. Hoffmann, M. Carlsen, B. Vad, A. Imparato, C. Rischel, and D. E. Otzen. Mechanical stress affects glucagon fibrillation kinetics and fibril structure. *Langmuir*, 27(20):12539–12549, 2011.

[21] C. L. Teoh, I. B. Bekard, P. Asimakis, M. D. W. Griffin, T. M. Ryan, D. E. Dunstan, and G. J. Howlett. Shear flow induced changes in apolipoprotein c-ii conformation and amyloid fibril formation. *Biochemistry*, 50(19):4046–4057, 2011.

[22] E. K. Hill, B. Krebs, D. G. Goodall, G. J. Howlett, and D. E. Dunstan. Shear flow induces amyloid fibril formation. *Biomacromolecules*, 7(1):10–13, 2006.

[23] A. Umemoto, H. Yagi, M. So, and Y. Goto. High-throughput analysis of ultrasonication-forced amyloid fibrillation reveals the mechanism underlying the large fluctuation in the lag time. *Journal of Biological Chemistry*, 289(39):27290–27299, 2014.

[24] J. H. Tan, D. D. Lin, S. Pillai, Y. Y. Zhang, B. Li, and X. F. Zhou. Ultrasound effects on assembly of glucagon fibrils. *Integrated Ferroelectrics*, 136:1–8, 2012.

[25] J. Zhong, M. J. Ma, J. Zhou, D. X. Wei, Z. G. Yan, and D. N. He. Tip-induced micropatterning of silk fibroin protein using in situ solution atomic force microscopy. *Acs Applied Materials & Interfaces*, 5(3):737–746, 2013.

[26] H. Yang, S. Y. Fung, M. Pritzker, and P. Chen. Mechanical-force-induced nucleation and growth of peptide nanofibers at liquid/solid interfaces. *Angewandte Chemie-International Edition*, 47(23):4397–4400, 2008.

[27] F. C. Zhang, F. Zhang, H. N. Su, H. Li, Y. Zhang, and J. Hu. Mechanical manipulation assisted self-assembly to achieve defect repair and guided epitaxial growth of individual peptide nanofilaments. *Acs Nano*, 4(10):5791–5796, 2010.

[28] Feng Zhang, Hai-Ning Du, Zhi-Xiang Zhang, Li-Na Ji, Hong-Tao Li, Lin Tang, Hua-Bin Wang, Chun-Hai Fan, Hong-Jie Xu, Yi Zhang, et al. Epitaxial growth of peptide nanofilaments on inorganic surfaces: Effects of interfacial hydrophobicity/hydrophilicity. *Angewandte Chemie International Edition*, 45(22):3611–3613, 2006.

[29] B. Dai, S. G. Kang, T. Huynh, H. Z. Lei, M. Castelli, J. Hu, Y. Zhang, and R. H. Zhou. Salts drive controllable multilayered upright assembly of amyloid-like peptides at mica/water interface. *Proceedings of the National Academy of Sciences of the United States of America*, 110(21):8543–8548, 2013.

[30] J. Chang, X. F. Peng, K. Hijji, J. Cappello, H. Ghandehari, S. D. Solares, and J. Seog. Nanomechanical stimulus accelerates and directs the self-assembly of silk-elastin-like nanofibers. *Journal of the American Chemical Society*, 133(6):1745–1747, 2011.

[31] S. Johnson, Y. K. Ko, N. Varongchayakul, S. Lee, J. Cappello, H. Ghandehari, S. B. Lee, S. D. Solares, and J. Seog. Directed patterning of the self-assembled silk-elastin-like nanofibers using a nanomechanical stimulus. *Chemical Communications*, 48(86):10654–10656, 2012.

[32] N. Varongchayakul, S. Johnson, Quabili T., J. Cappello, H. Ghandehari, S.D. Solares, W. Hwang, and J. Seog. Direct observation of amyloid nucleation under nanomechanical stretching. *Acs Nano*, 7(9):7734–7743, 2013.

[33] S. Lenhert, C. A. Mirkin, and H. Fuchs. In situ lipid dip-pen nanolithography under water. *Scanning*, 32(1):15–23, 2010.

[34] C. C. Wu, D. N. Reinhoudt, C. Otto, A. H. Velders, and V. Subramaniam. Protein immobilization on ni(ii) ion patterns prepared by microcontact printing and dip-pen nanolithography. *Acs Nano*, 4(2):1083–1091, 2010.

[35] J. Zhong, G. Sun, and D. N. He. Classic, liquid, and matrix-assisted dip-pen nanolithography for materials research. *Nanoscale*, 6(21):12217–12228, 2014.

[36] K. A. Brown, D. J. Eichelsdoerfer, X. Liao, S. He, and C. A. Mirkin. Material transport in dip-pen nanolithography. *Frontiers of Physics*, 9(3):385–397, 2014.

[37] Santiago D. Solares, Jonathan Chang, Joonil Seog, and Adam U. Kareem. Utilization of simple scaling laws for modulating tip-sample peak forces in atomic force microscopy characterization in liquid environments. *Journal of Applied Physics*, 110(9), 2011.

[38] John Melcher, Xin Xu, and Arvind Raman. Multiple impact regimes in liquid environment dynamic atomic force microscopy. *Applied Physics Letters*, 93(9), 2008.

[39] G. C. Yang, M. K. Wong, L. E. Lin, and C. M. Yip. Nucleation and growth of elastin-like peptide fibril multilayers: an in situ atomic force microscopy study. *Nanotechnology*, 22(49), 2011. Yang, Guocheng Wong, Michael K. Lin, Lauren E. Yip, Christopher M.

[40] Edward D Palik. *Handbook of optical constants of solids*, volume 3. Academic press, 1998.

[41] Anita I Bailey and Susan M Kay. Measurement of refractive index and dispersion of mica, employing multiple beam interference techniques. *British Journal of Applied Physics*, 16(1):39, 1965.

[42] P. J. Sides, D. Faruqui, and A. J. Gellman. Dynamics of charging of muscovite mica: Measurement and modeling. *Langmuir*, 25(3):1475–1481, 2009.

[43] T. J. Senden and C. J. Drummond. Surface-chemistry and tip sample interactions in atomic-force microscopy. *Colloids and Surfaces a-Physicochemical and Engineering Aspects*, 94(1):29–51, 1995.

[44] Keith A Brown, Daniel J Eichelsdoerfer, Wooyoung Shim, Boris Rasin, Boya Radha, Xing Liao, Abrin L Schmucker, Guoliang Liu, and Chad A Mirkin. A cantilever-free approach to dot-matrix nanoprinting. *Proceedings of the National Academy of Sciences*, 110(32):12921–12924, 2013.